UTILIZATION OF FRICTION STIR PROCESSING TO IMPROVE THE MECHANICAL PROPERTIES OF GAS METAL ARC WELDED 5083 ALUMINUM ALLOY PLATES

A THESIS SUBMITTED TO
THE GRADUATE SCHOOL OF NATURAL AND APPLIED SCIENCES
OF
MIDDLE EAST TECHNICAL UNIVERSITY

BY

SHAHIN TAKHT FIROUZEH

IN PARTIAL FULFILLMENT OF THE REQUIREMENTS
FOR
THE DEGREE OF MASTER OF SCIENCE
IN
METALLURGICAL AND MATERIALS ENGINEERING

FEBRUARY 2016

Approval of the thesis:

UTILIZATION OF FRICTION STIR PROCESSING TO IMPROVE THE MECHANICAL PROPERTIES OF GAS METAL ARC WELDED 5083 ALUMINUM ALLOY PLATES

submitted by **SHAHIN TAKHT FIROUZEH** in partial fulfillment of the requirements for the degree of **Master of Science in Metallurgical and Materials Engineering Department, Middle East Technical University** by,

Prof. Dr. Gülbin Dural Ünver _____
Dean, Graduate School of **Natural and Applied Sciences**

Prof. Dr. C. Hakan Gür _____
Head of Department, **Metallurgical and Materials Engineering**

Prof. Dr. C. Hakan Gür _____
Supervisor, **Metallurgical and Materials Engineering Dept. METU**

Examining Committee Members:

Prof. Dr. Rıza Gürbüz _____
Metallurgical and Materials Eng. Dept. METU

Prof. Dr. Bilgehan Ögel _____
Metallurgical and Materials Eng. Dept. METU

Prof. Dr. C. Hakan Gür _____
Metallurgical and Materials Eng. Dept. METU

Assist. Prof. Dr. Kazım Tur _____
Metallurgical and Materials Eng. Dept. Atılım University

Assist. Prof. Dr. Mert Efe _____
Metallurgical and Materials Eng. Dept. METU

Date: 04.02.2016

I hereby declare that all information in this document has been obtained and presented in accordance with academic rules and ethical conduct. I also declare that, as required by these rules and conduct, I have fully cited and referenced all material and results that are not original to this work.

Name, Last name: Shahin TAKHT FIROUZEH

Signature

ABSTRACT

UTILIZATION OF FRICTION STIR PROCESSING TO IMPROVE THE MECHANICAL PROPERTIES OF GAS METAL ARC WELDED 5083 ALUMINUM ALLOY PLATES

Takht Firouzeh, Shahin

M. S., Department of Metallurgical and Materials Engineering

Supervisor: Prof. Dr. C. Hakan GÜR

February 2016, 85 pages

Fatigue failure of the welded structures is a major problem in engineering applications. It is known that the heat affected zone (HAZ) of the welded Al-alloys is prone to fail due to coarse microstructure and poor mechanical properties. Therefore, any improvement in HAZ may extend the service life of the welded component. The hypothesis of this study is that localized application of friction stir processing (FSP) before welding may improve the mechanical properties of HAZ, and thus, may reduce the fatigue crack growth rate. The 5083 Al-alloy plates were joined by following two different routes: application of gas metal arc welding in a conventional way, and application of gas metal arc welding after FSP of the bevel zones of the plates which are going to be affected by heat input. To investigate the improvements, hardness, tensile and fatigue crack propagation tests were performed, and microstructures and fracture surfaces were investigated by optical and electron microscopy.

Keywords: Friction Stir Processing, Gas Metal Arc Welding, Heat Affected Zone, Mechanical Properties, Fatigue Crack Growth Rate

ÖZ

GAZ METAL ARK KAYNAĞI İLE BİRLEŞTİRİLMİŞ 5083 ALÜMİNYUM ALAŞIMI PLAKALARIN MEKANİK ÖZELLİKLERİNİN GELİŞTİRİLMESİ İÇİN SÜRTÜNME KARIŞTIRMA PROSESİNİN KULLANILMASI

Takht Firouzeh, Shahin
Yüksek Lisans, Metalurji ve Malzeme Mühendisliği Bölümü
Tez Yöneticisi: Prof. Dr. C. Hakan Gür

Şubat 2016, 85 sayfa

Kaynaklı yapılardaki yorulma hasarı, mühendislik uygulamalarında karşılaşılan temel sorunlardan biridir. Kaynaklanan Al-alaşımlarında ısıdan etkilenen bölgenin iri taneli içyapısı ve zayıf mekanik özellikleri nedeniyle yorulma hasarlarına yatkın olduğu bilinmektedir. Bu nedenle, ısıdan etkilenen bölgede yapılacak herhangi bir iyileştirme, kaynaklı yapının kullanım ömrünü uzatacaktır. Bu çalışma, kaynak öncesinde plakaların kaynak hazırlık bölgelerine sürtünme karıştırma işlemi uygulanarak, kaynak sonrasında oluşan ısıdan etkilenen bölgenin mekanik özelliklerinin iyileşeceği ve yorulma çatlağı ilerleme hızının düşürülebileceği hipotezine dayanmaktadır. Deneysel çalışmalarda, 5083 alüminyum alaşımı plakalara iki farklı yöntem uygulandı: birinci yöntemde plakalar gaz metal ark kaynağı ile birleştirildi, ikinci yöntemde ise kaynak ısı girdisinden etkilenecek kaynak ağzı bölgesine sürtünme karıştırma işlemi uygulandıktan sonra gaz metal ark kaynağı yapıldı. Özelliklerdeki iyileşmeleri tespit etmek için sertlik, çekme ve yorulma çatlağı ilerleme testleri gerçekleştirildi; mikroyapılar ve kırılma yüzeyleri optik mikroskop ve elektron mikroskobu ile incelendi.

Anahtar Kelimeler: Sürtünme Karıştırma Prosesi, Gaz Metal Ark Kaynağı, Isıdan Etkilenen Bölge, Mekanik Özellikler, Yorulma Çatlağı İlerleme Hızı

To My Teachers

ACKNOWLEDGMENTS

I am deeply thankful to my supervisor Prof. Dr. C. Hakan GÜR, for his generous efforts, trust and guidance.

Invaluable directions, motivations and positive attitude of Dr. Süha TİRKEŞ and Dr. Koray YURTIŞIK is highly appreciated.

Without precious efforts and sincere support of Mrs. Günseli AKÇAY, Mr. Göksu GÜRER, Mr. Mertcan BAŞKAN, Mr. Tolga ERTÜRK, Mrs. Burcu TOLUNGUÇ, Mrs. Mine KALKANLI, Mr. Atalay ÖZDEMİR, Mr. Cemal YANARDAĞ and Mr. Orhan AYDIN, progression within the study would not be possible. It was a pleasure to cooperate with them.

I am grateful for supports of METU Welding Technology and NDT Center, and NOKSEL Boru Sanayi A.Ş.

The fellowship of METU Rugby teammates and METU swimming pool athletes was one of the most delightful assets in this period.

My Family was my strongest motivation source to accomplish my studies.

TABLE OF CONTENTS

LIST OF TABLES

TABLES

LIST OF FIGURES

FIGURES

CHAPTER 1

INTRODUCTION

Aluminum is a commonly used material in industry because of its lightweight, corrosion resistance, recyclability and strength. Among its alloys, 5083-H111 is an ideal alloy for production of armor and marine vehicles because of its weldability, reduced sensitivity to hot cracking and moderate strength. For joining of the parts gas metal arc welding (GMAW) is a preferred technique because of its feasibility. However, the drawbacks of this method such as coarsening of grains and precipitation in HAZ, limit the mechanical properties of the weldments. When the dynamic loads on the on the welded structures are taken into account, crack initiation and propagation is likely to happen at HAZ.

Better mechanical properties can be achieved, maintaining finer grains and equiaxed microstructure (high-angle grain boundaries) [1]. These properties are obtainable with means of continuous dynamic recrystallization. Utilization of conventional thermo mechanical processes is not an asset for this purpose. This is due to the high stacking fault energy of aluminum which ease the cross slip of screw dislocation being caused to occurrence of recovery in expense of recrystallization [2].

Friction stir processing (FSP), is an adaptation of friction stir welding (FSW) [2]. It has been applied of as an improvement technique in this study. FSP is a severe deformation process which modifies the microstructure by means of dynamic recrystallization. Trials of FSP on cast aluminum alloys have shown a tremendous decrease in grain and precipitation size [3]. The final microstructure is observed to be equiaxed. The strain energy obtained from mechanical work of tool rotation and

travelling is used up for recovery and recrystallization of the former grains facilitating the temperatures above the recrystallization temperature of material [2].

While such a microstructure is obtained, the effect of weld heat on its mechanical properties is expected to be less than the effect on mechanical properties of H111 temper. An MSc. thesis on post FSP of weld metal using the same material has already been completed, and a remarkable improvement in mechanical properties was obtained [4].

The theory topics of this study are presented in Chapter 2. The procedures of FSP and GMAW which were applied on the 20 mm thick plates of 5083-H111 aluminum alloy are given. Optimization trials, microstructural investigations, tensile, hardness and crack propagation tests were performed. The methodology is explained in Chapter 3. Images from the microstructure of specimens, stress-strain diagrams, hardness profiles, crack size versus number of cycle curves and da/dN versus ΔK curves are presented. Fractured surfaces were investigated using scanning electron microscopy. The improvements are pointed out and the results are discussed in Chapter 4.

CHAPTER 2

THEORY

2.1. Properties of 5083, Aluminum Alloy

In Aluminum alloy system, the first digit is to illustrate the alloying element. Second digit shows the variation in original basic alloy. The third and fourth digit designates the specific alloy within the series.

The main alloying element of the 5083-H111 Aluminum alloy is magnesium. It is the 83rd variation of the basic alloy which has been subjected to some work hardening but, not as much as required for H11 (Table 2.1). The number following H1 indicates degree of strain hardening [5].

Considering the binary phase diagram of aluminum and magnesium, (Figure 2-1) the slope of the solvus line is positive. Although this makes 5xxx series suitable for precipitation hardening, the problem of formation face centered cubic Al_3Mg_2, prevents the commercialization [6]. Therefore, it is categorized as non-heat treatable alloys.

The effect of Magnesium addition on tensile yield strength and elongation amount is illustrated in Figure 2-2. Magnesium in 5xxx improves corrosion resistance and strength via solution strengthening. Addition of Manganese, also presents good amount of formability. Besides, formation of Al_6(Mn, Fe) and Al_{12}(Mn, Fe)$_3$Si by eutectic reaction, retard the recrystallization and controls the grain size [6].

The most observed second-phase particles are stated to be Mg_2Si and Al_6(Mn, Fe).

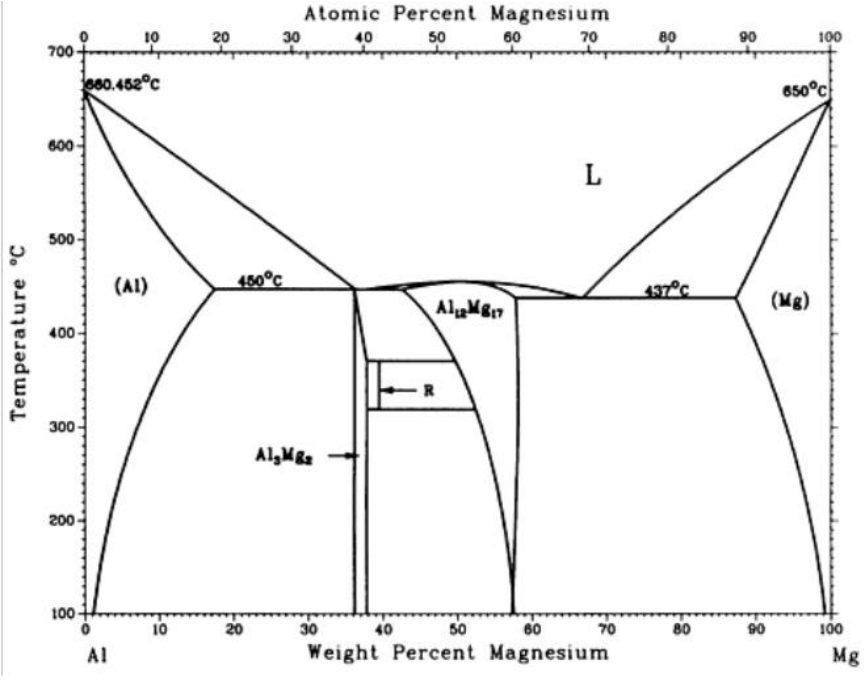

Figure 2-1. Binary Aluminum-Magnesium Phase Diagram [7]

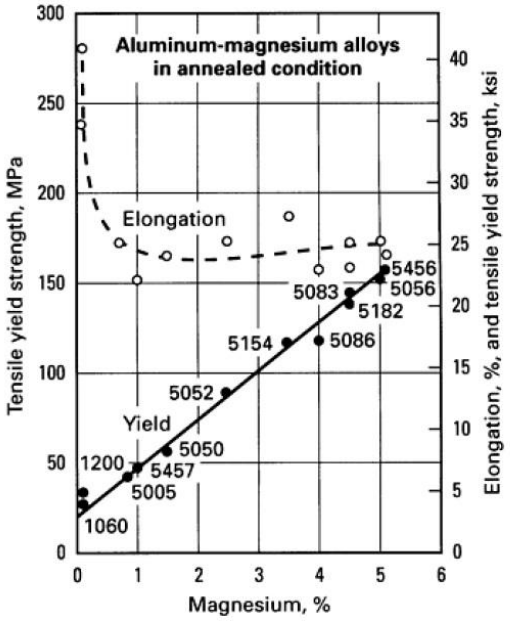

Figure 2-2 Effect of Magnesium addition on Strength of Al 5xxx [8]

The variation of the tensile strength is given in Table 2.1.

Table 2.1. Mechanical properties of 5083 Al-alloy at different tempers; O: As-cast and Annealed, H1: Strain Hardened Only, H3: Strain Hardened and Stabilized [8]

Temper	**Yield strength MPa**	**Tensile strength MPa**	**Elongation %**
O	145	290	22
H112	193	303	16
H116	228	317	16
H321	228	317	16
H323, H32	248	324	10
H343, H34	283	345	9

Table 2.2. Mechanical properties of 5083 Al-alloy at various temperatures [8]

Temperature °C	**Yield Strength (0.2% offset) MPa**	**Tensile Strength MPa**	**Elongation %**
-195	165	405	36
-80	145	295	30
-30	145	290	27
25	145	290	25
100	145	275	36
150	130	215	50
205	115	150	60

2.2. Joining of Aluminum Alloys

Heat input during welding of aluminum alloys, remarkably affects the microstructure and mechanical properties of the heat affected zone (HAZ) due to excellent heat conductivity [6]. Although formation of the HAZ is inevitable, some modifications such as formation of fine and equiaxed grains, breaking-up and uniform distribution of precipitates, are required to minimize the negative effects.

Generally, the heat is applied locally to edges that are going to be welded. The energy input (H), is in arc welding is calculated as follows:

$$H = EI/V \quad (1)$$

where: E = volts, I = amperes, V = Travel velocity of heat source (mm/sec)

To calculate the H_{net}, H has to be multiplied with the heat transfer efficiency, which is between 0.8 and 1.0. In order to melt the filler and base metal during the arc welding, an amount of heat Q is needed. This quantity is the sum of heat needed to elevate the metal temperature to melting temperature and the heat needed to melt the solid:

$$Q = (T_m+273)2 / 300000 \ [J/mm^3] \quad (2)$$

where T_m is the melting temperature of the welded material in °C.

Because of heat input three regions exist:

- Volume of the weld metal, which consists of molten base metal and the filler metal (WM),
- Heat affected zone (HAZ),
- Un-effected base metal (BM).

In most of the arc welding methods the arc is used as the source of the heat. This arc is normally formed with a current of 250 A and voltage of 25 V. The efficiency of arc welding methods is between 20% and 85%.

Gas metal arc welding (GMAW) utilizes a continuous filler wire which is fed by nozzle into the weld pool. The shielded gas is also blown by the nozzle. The energy is provided by power supply, which produces the arc and heat needed to melt the filler wire and base metal. In order to maintain a stable, spatter free and axial spray, spray arc transfer is used for welding of thick pieces. In this method, a portion of molten metal is taken by spray arc and it is sprayed to the base metal from the electrode wire. Argon-helium remix gas is used in this method for aluminum and its alloys due to large pool size. The choice of electrode is an important matter. The filler material has to match the base metal or even enhance its properties.

While heat treatable alloys are more sensitive to the heat of fusion welding, according to previous studies, dramatic drops of tensile strength and endurance of alloys in HAZ region of non-heat treatable alloys are observed [9] [10]. Hadadzadeh et al, measured a drop up to 50 MPa in both tensile and yield strengths of HAZ region in Aluminum 5083-H111.

2.3. Friction Stir Processing

Friction stir processing (FSP) was invented a decade after invention of friction stir welding (FSW) in 1991. FSW is a complex solid-state welding technique which is favorable in many terms. It is mostly applicable to metals with superplastic behaviors during butt welding. However it is not commonly used because of higher cost and difficulty in application. FSP is a modification of FSW, with the same methodology, which is a regional refinement method. It is conducted to maintain better properties, due to the changes on microstructure.

In these processes (FSW and FSP), there is a rapidly rotating tool plunged into the material, until the shoulder is in firm contact with the surface of material. Then, the tool starts to travel in the process/ weld line. This contact and also the flow of the material around the tool cause the formation of heat, which decreases the flow stress of the

material. The softened, plasticized material is easily transported from upfront of the tool into its backward, where material is forged to the elderly transported material. The temperature of the material does not reach to its melting temperature, as this hot-shear deformation process happens. This process causes the formation of an asymmetric profile of the process/weld line. Therefore, advancing and retreating sides are defined and formed in process/ weld profile. Both sides differ by the heat transfer from them, their material flow characteristics and somehow hardness values. Also, three different regions observed in this process are nugget zone (NZ), thermo-mechanically affected zone (TMAZ) and the HAZ. Dramatic changes in the microstructure of these regions are observed (especially NZ).

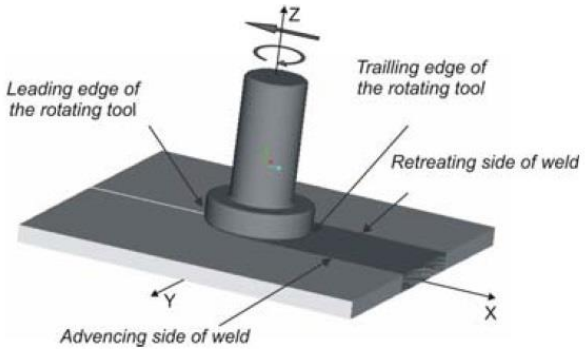

Figure 2-3 Directions in FSW/P

Obtaining fine and equi-axed grains and broke-up of precipitations uniformly dispersed in structure, are the main and desired results observed. Friction stir processing of cast aluminium alloys results in refinement of matrix grains, break-up of coarse dendrites, fragmentation of secondary phases and uniform distribution of secondary particles [11] [12]. All of these provide enough motivation to maintaining such a microstructure that will omit the main post-welding problems in HAZ of arc welded specimens. FSP, generally speaking, is a process including forging and extrusion with higher rates of strain during which, dynamic recrystallization phenomena is happening. There are

many parameters which affect the quality of the process in different manners. The most important parameters are rotational and transverse speeds and tool geometry [13] [14].

2.3.1 Forces

During FSP, three forces are applied on the tool. These are the forces in the x, y and z direction as shown in Figure 2-3. Studying the magnitude, direction and the changes of these forces is important to get familiar with the deformational characteristics of the process. In their study, Zimmer and others [15] have measured the amount of forces created during FSW of 6mm thick 6000 series aluminum plate. The generated torque has also been measured and it is stated that there are six steps in which force and torque amounts are subjected to change. These measurements and steps are illustrated in Figure 2-4. It is obvious that the maximum force amount is measured in z-direction which explain the urge of the material to flow out. However, the increase in the cross-section are of the shoulder may prevents this issue.

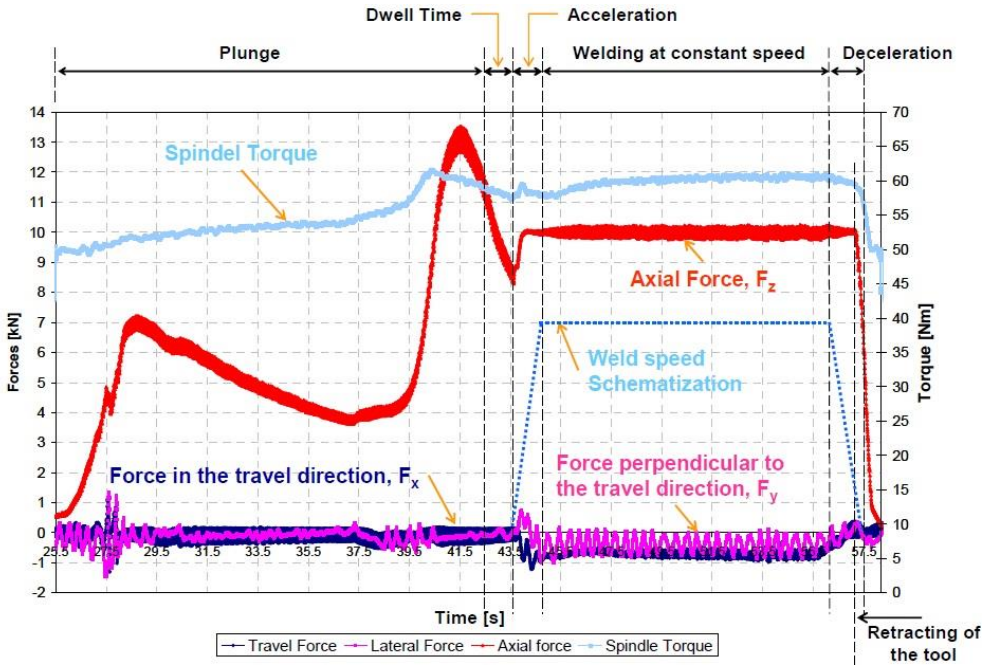

Figure 2-4. Force and torque vs. time measurements for FSP [19]

The plate thickness in this study is 20mm, which is going to be processed from both sides by a 9mm long pin. Therefore, it is roughly approximated that, these forces are going to be doubled in this case. In addition, the experiments at Zimmer's work has done using a simple geometry tool design which has not as much sharp corners and threads as the Triflat tool used in this study. Thus, even higher force magnitudes is expected.

Also, the forces are directly affected by the rotational speed and travel speed of the tool. As the travel speed increases and rotational speed decreases the force magnitudes are increased [16]. Also in Figure 2-5, for different plunging speeds and travel speeds the axial force and torque amount is illustrated.

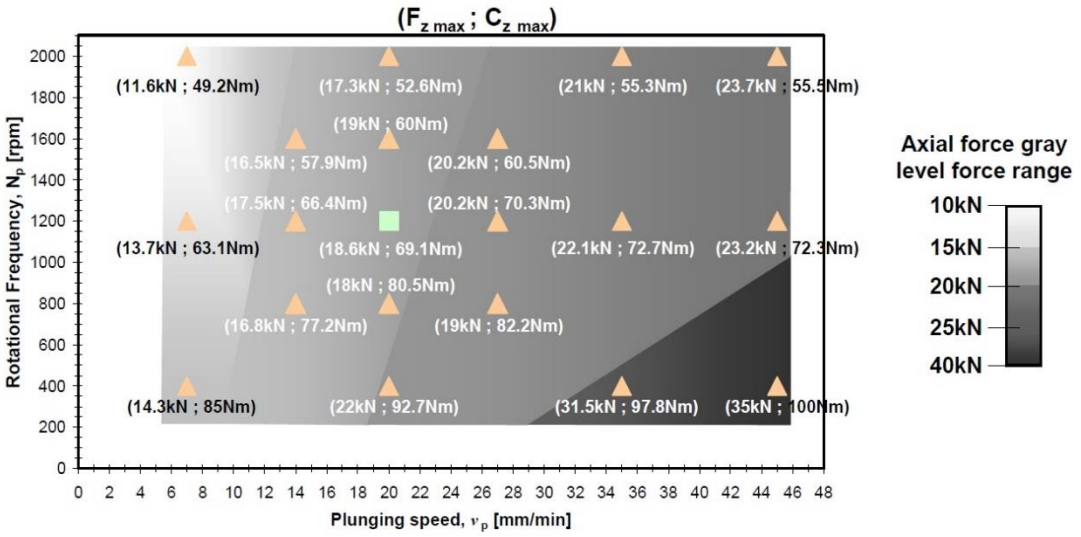

Figure 2-5. Magnitudes of force and torque for different speed parameters [15]

2.3.2 Material Flow

The flow of material around the tool is probably the most important phenomenon that defines the characteristics of the process. For different friction coefficients, various flow patterns can be observed, and stress and strain amounts are directly related to

material flow. Most of the occuring defects during the FSP is due to material flow behavior.

Most of the material flow studies were pusued by the marker method as Figure 2-6 or simulation methods.

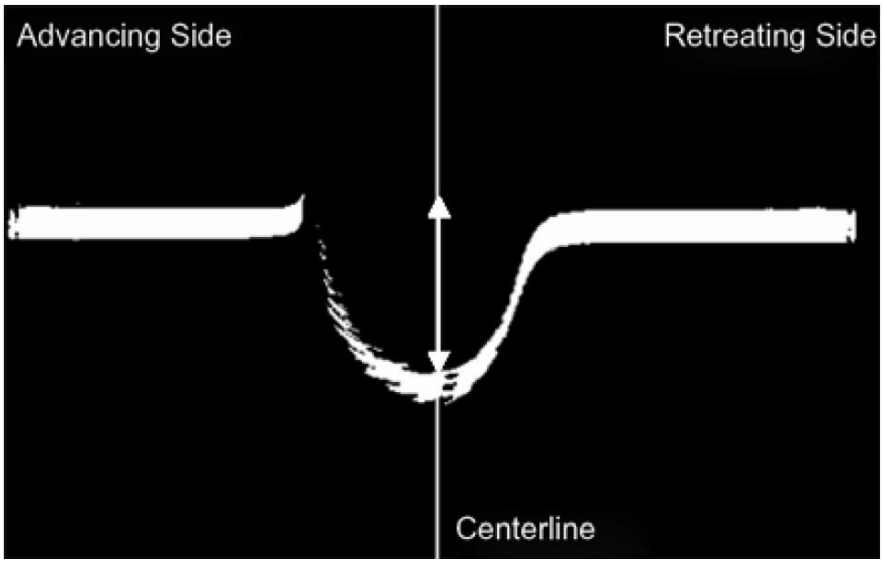

Figure 2-6. Marker study to observe the final flow after passing of probe [17]

In their work, Schmidt et al. have concluded that the thickness of the shear zone around the tool is equal to advancing distance per evolution of the pin [18]. It can be stated that maximum backward material transport (at the weld/ process centerline) is approximately equal to the probe diameter. Also, shear zone must contain a greater volume of material than it is needed to be transferred in each revolution. Most of the material flow occurs through the retreating side and the transport of the plasticized material behind the tool forms the united joint.

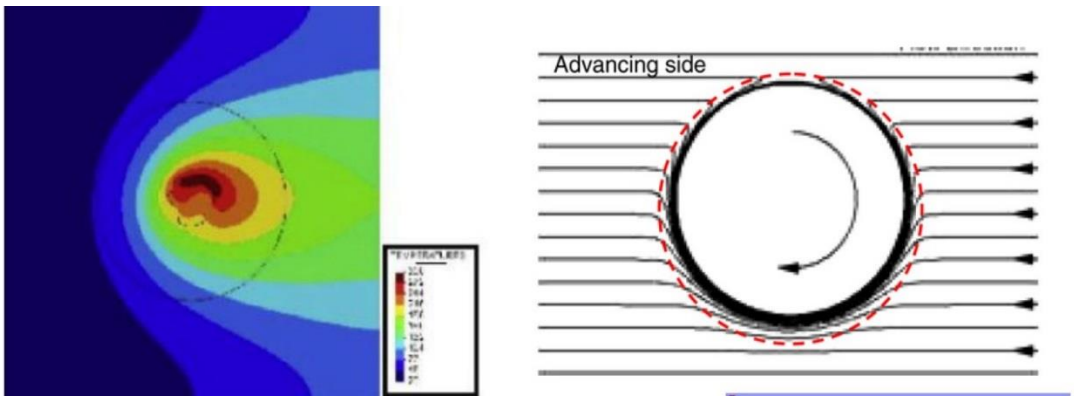

Figure 2-7. Instantaneous temperature profile during fsp, and shear zone around the pin [19]

In the studies that have been mentioned above, only the two dimensional flows are studied and illustrated. During the process, however, there are different kinds of flows of plasticized material when the plate is taken to the account as a three dimensional process. First, near the tool, a slug of plasticized material rotates around the tool. This motion is driven by the rotation of the tool and the resulted friction between the tool and the work-piece. Second, rotational motion of the threaded pin tends to push material downward close to the pin which drives an upward motion of an equivalent amount of material somewhat farther away. Finally, there is a relative motion between the tool and the work piece [17].

Characteristics of the material flow are worth to study since, it is responsible for heat formation and strain amounts. Therefore it will give enough knowledge to control the process in order to get adequate results.

2.3.3. Stresses and Strains

The forces applied on the material can vary vastly with respect to stages of process or weld. Measuring stress and strains in the processed zone is the main prequisite to determine the deformation processing of material. In FSP, extrusion and forging are the main issues for processing of the metal at high strain rates. Strain rates can vary also,

with respect to variation of FSP parameters and tool geometry. Amount of strain rate is one of the important factors in grain size of stirred zone during the dynamic recrystallization process. In their study for instance, Jata and Semiatin estimated a typical deformation strain rate of 10 s^{-1} by measuring grain-size and using a correlation between grain-size and Zener–Holloman parameter which is temperature compensated strain rate [20]. Kokawa et al. estimated an effective strain rate in stir zone in the range of 2–3 s^{-1} [10].

The strain rate was found to correlate with the flow stress and temperature as given in [21]:

$$\dot{\varepsilon} = A(sinh\alpha\sigma_e)^n exp(-\frac{Q}{RT}) \quad (3)$$

Where A, n and α, are material constants. Although they are functions of strain during the work-hardening, these values get independent of it when a steady state of strain is maintained and work hardening gets balanced with the recovery mechanism and softening effect is maintained. This phenomena happens before the strain is equal to a low value of 1. Since in FSP strain is much higher, a single set of material constant with the assumption of being independent of strain can be used. Also, the apparent activation energy Q are derived by fitting the equation to experimental data, and are all independent of temperature. R is the gas constant and T stands for temperature.

Rearranging this expression effective stress can be written as

$$\sigma_e = \frac{1}{\alpha} sinh^{-1}[(\frac{Z}{A})^{\frac{1}{n}}] \quad (4)$$

Where, $Z=\dot{\varepsilon}exp(Q/RT)$ is known as the Zener–Holloman temperature compensated strain rate [22] [23] [24].

2.3.4 Defects

The main defects in FSW/P are porosities or surface defects. As two of the most affecting parameters of FSW/P, rotational and travel speeds have a big role in

formation of these defects. For example keeping the rotational speed constant, increasing the travel speed can cause wormholes created behind the pin in bottom regions. As, the travel speed is increased, the number of wormholes are also increased. It is because of the weak joining of the material resulted from inadequate material flow. Generally, lower rotational over travel speed may cause formation of Wormholes near the bottom.

Also in order to prevent the changes in microstructure, heat flow should be homogeneous around the tool in order to have the same heat treatment all over the processed area.

Another important fact is that, most of the cracks and porosities are observed around the advancing side of the tool. An analogy with machining process of different metals which is shown in Figure 2-8, can explain this issues. If the material has enough ductility and a flow stress below the needed value created by heat, a proper and continuous joining can happen.

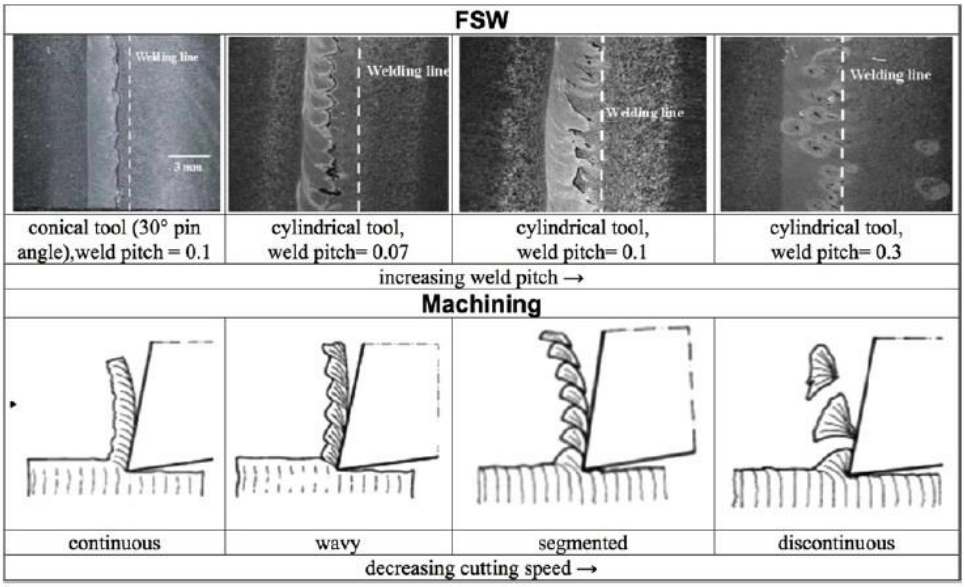

Figure 2-8. Analogy between chip morphology in machining and material flow in FSW [11]

2.3.5 Residual Stresses

Residual stresses can be advantageous and hazardous. In FSP/W residual stresses are created by mechanical and thermal effects. In the worst case, up to half of the ultimate tensile strength is observed along the stirred line. Which necessiates some small amount of compressive residual stresses at HAZ of the workpiece.

In Figure 2-9, a typical surface residual stress distribution after FSW/ P is illustrated. Application of tensioning during the process may result in compressive residual stresses at the processed/ welded line. Richards et al. has shown that stretching at a level of 50% tensile strength during FSP/ W created compressive residual stresses and therefore, improvement in the crack propagation behavior [25] [26].

Generally, higher rotational speeds and lower transverse speeds, both increase residual stresses.

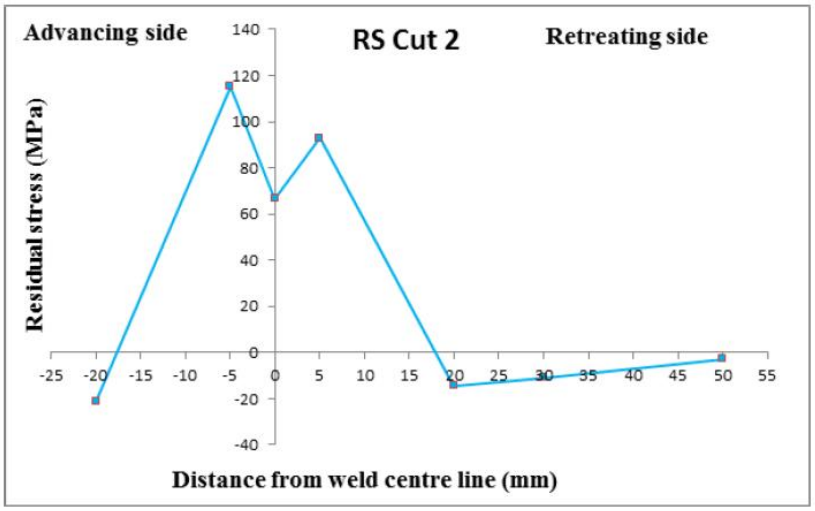

Figure 2-9. A typical residual stress vs. distance diagram for FSP/W [25]

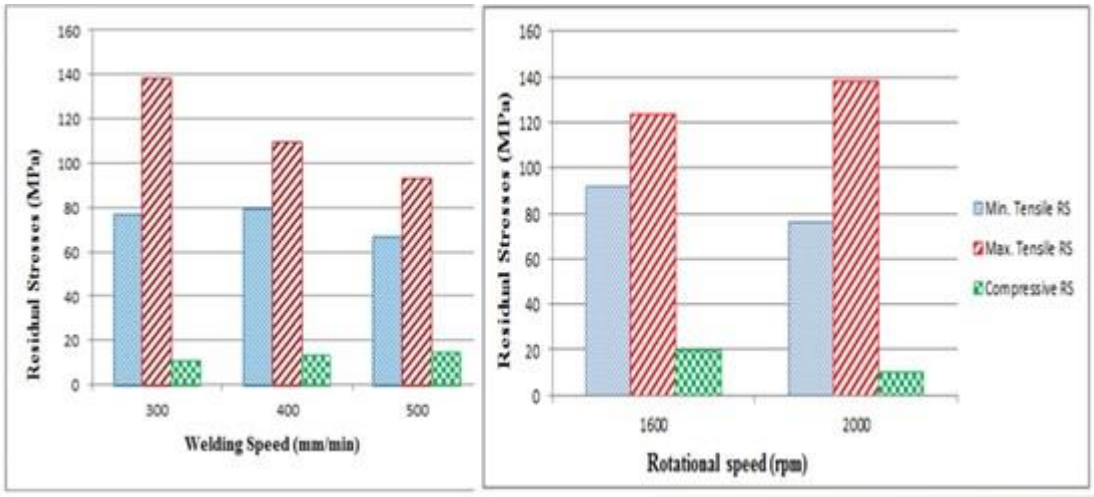

Figure 2-10. Variation of residual stresses with travel speed and rotational speed [25]

2.3.6 Microstructure

During FSP/W, dynamic recrystallization occurs. Thus, the final recrysalized microstructure is finer than the original microstructure (Figure 2-11). As the tool reaches the region of processing, at first high amount of plastic work is applied on microstructure. This leaves the material with a highly deformed microstructure and high stored energy inside. This energy is the driving force for further steps. Since recovery and recrystallization is time and temperature dependant, elevated tempratures makes the driving force to proceed the recovery of the deformed microstructure. At this period subgrains are formed. As time passes, these subgrains get rid of the dislocations. Subsequently, growth can happen. At final steps of recrystallization, new strain free and fine grains are formed. In case, the temprature is enough and material is kept at moderately elevated temperatures for some time, further continuos growth of grains takes place and coarsening happens.

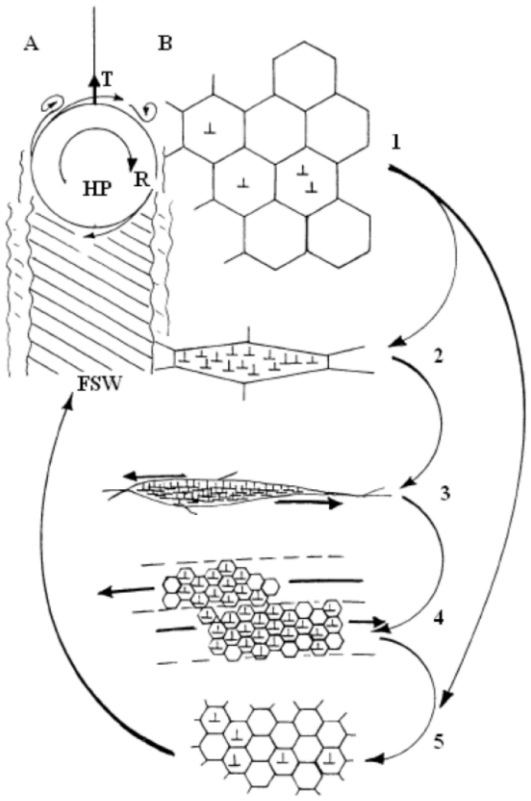

Figure 2-11. Recrystallization of microstructure after tool stirring the region [11]

Final grain size - although it is not the most important issue in FSW - is the main characteristic and goal of the FSPed product. It is depended on many different factors such as tool geometry, reached temperature and number of passes. Within optimum conditions, 3 micron equiaxed grains are obtained in earlier studies and primary coarse intermetallics are reported to get finer and dispersed more homogeneously [27]. In Figure 2-12, a diagram of the grain boundary size vs. temperature of process is shown.

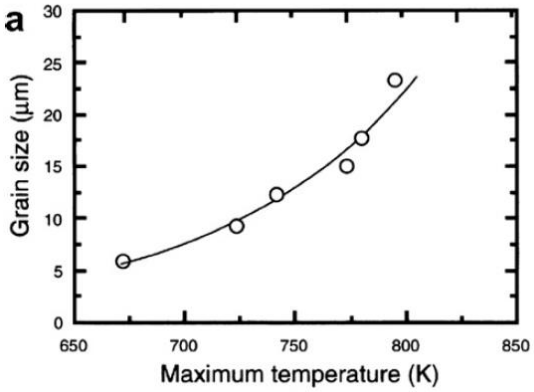

Figure 2-12. Change of grain size during FSP [19]

As a microstructure property, superplasticity of the FSP/W-ed material is another outcome of the process. Briefly speaking, the criteria for superplastic material is provided when fine grain size, equiaxed grains and strain free microstructure is existing. FSP/W is a process which provides all of these properties at once when performed at adequate conditions.

2.4. Crack Growth

The cracking is normally started at discontinuities or plastic strain accumulations in the form of slip bands on the surface. Amount of stress concentration is an important factor in initiation of the crack. Although in some cases the life of a material only consists of crack propagation, because of the pre-existing defects, normally the service life is the sum of crack initiation and propagation stages.

When the stress at tip of the crack is in a specific range, the crack will grow at each cycle. These cycles form microscopic footprints on the fracture surface, which are called striations. Striations are mostly observed in ductile metals. The amount of the load and the amplitude amount are the most important factors in determination of the cycle numbers, N_f, before failure.

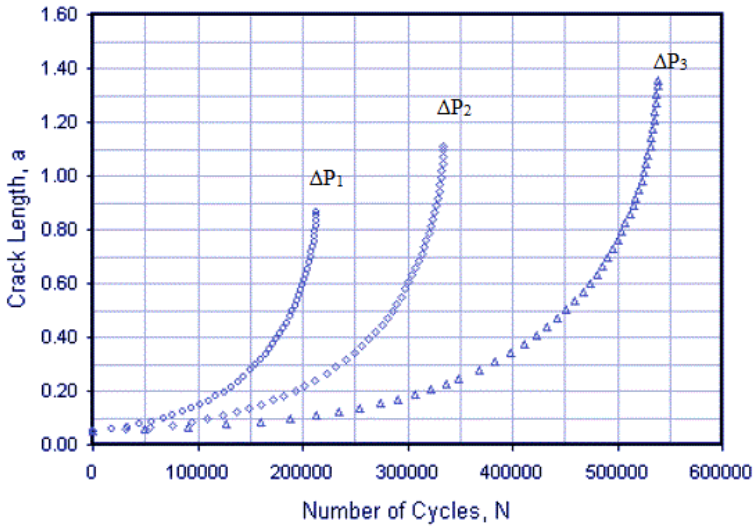

Figure 2-13. S-N curves - Crack growth rates for different load amplitudes [28]

To investigate the behavior of the crack, different approaches are utilized. One of these analytical procedures is the linear elastic fracture mechanics (LEFM). The stress in the crack tip is correlated to nominal stress on the specimen, crack geometry, growth rate and the resistance of the material. To find the stress state in vicinity of crack, therefore, a factor of stress intensity K has been defined. Based on assumptions of LEFM, the stress amount is leaded to infinite values in the crack tip. On a given constant load amplitude (ΔP), load ratio (R) and cyclic frequency (v), the crack size (a) will increase with the number of the cycles (N). On their work Paris and Erdogan [29], revealed the correlation between da/dN and the stress intensity parameter of the cycles. It was suggested that ΔK determines the stresses in crack tip and it includes the ΔP and a. Therefore following equation was derived:

$$\left(\frac{da}{dN}\right)_{R,v}=f(\Delta P, a) \quad (5)$$

$$\frac{da}{dN} = C(\Delta K)^m \quad (6)$$

When the log-log graph of ΔK and da/dN is drawn (Figure 2-14), C and m values can be calculated from the linear second region which is called power law region. In region I, the crack does not grow until ΔK reaches the threshold value. At the initiation, the crack propagates at high shear stress planes which have a 45 degrees orientation to the axial load. At these stages the refined grains and secondary particles are very helpful to block the crack. They act as microstructural barriers. Then crack size changes rapidly until it is calmed down in the second region, where the slips start to form in other planes close to crack tip. This results in growth of crack perpendicular to load direction. The third region is where crack has enlarged and crack is leaded to failure [30] [31].

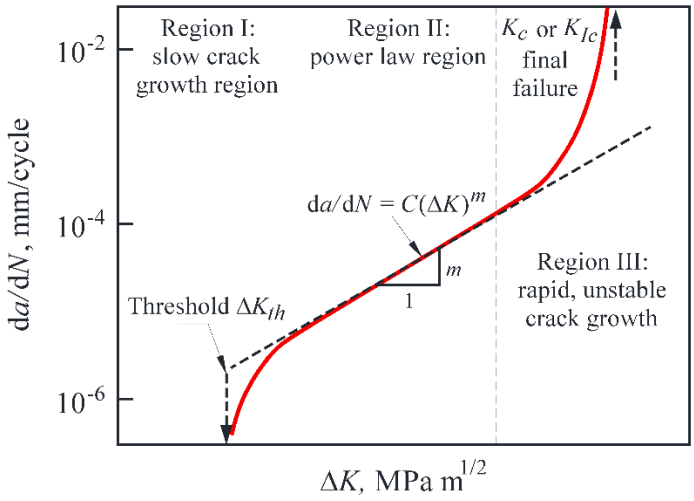

Figure 2-14. Logarithmic crack growth rate [32]

The linear equation of the stage II, according to Paris law can be written as below:

$$log\frac{da}{dN} = log\,C + m\,log(\Delta K) \qquad (7)$$

According to equation 7, the values of m and C can be easily calculated by finding the slope of the da/dN versus ΔK curve for m and the interception at y-axis to find the value of C.

Another important factor in crack initiation and growth is the stress ratio value ($R=P_{min}/P_{max}$). Since R is directly related to K_{max} and K_{min} values, it defines the effective ΔK (ΔK_{eff}) amount. ΔK_{eff} also, has a critical role in crack closure mechanism, which can happen through different situations. Plastic deformation at crack tip or contact point of fracture surface, i.e. secondary particles are two instances. The common characteristic of crack closure mechanism is reducing the ΔK_{eff}. When the crack surfaces are touching each other before the K_{min} value is reached, the ΔK range is simply derogated [31].

2.5. Effects of Multi-pass FSP and Heat Treatment of FSPed Plates

The consequences of multi-passing FSP technique have been investigated in study of Chen et al. [33]. In this study, usage of overlapping technique caused one third of the FSPed region to be subjected to double-passing. The effect of three consecutive FSP passes (100% overlap) on 3.5mm thick Al-5083 plates was studied for two parameter sets with constant travelling speed of 360 mm/min and rotational speeds of 600 rpm and 1200 rpm. Slightly coarser grains have been observed for higher heat input (1200 rpm, 360 mm/min). However, a significant change has not been occurred in the grain size of the nugget zone after the third pass (Figure 2-15).

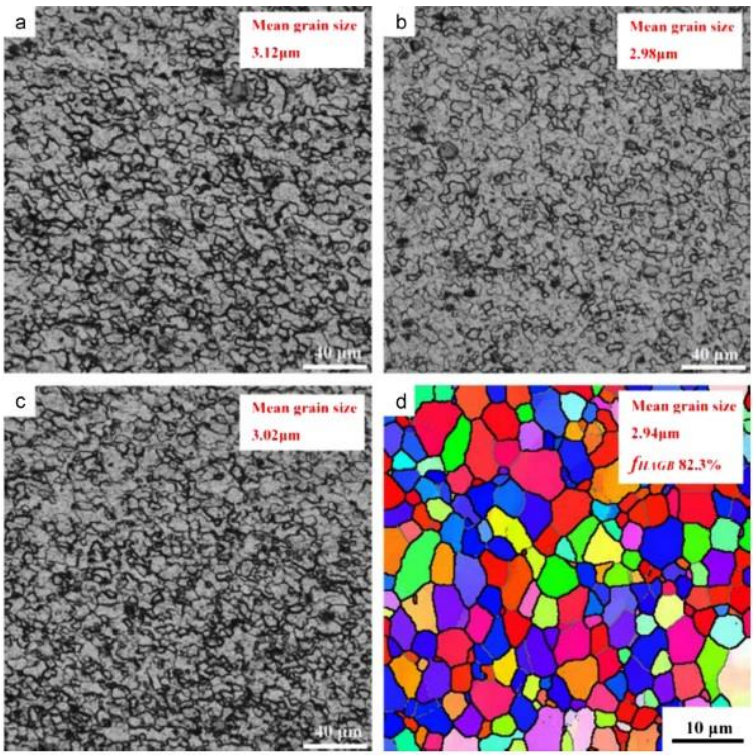

Figure 2-15. The evolution of nugget zone microstructure during multi-passing (a) First pass, (b) Second pass (c) Final pass, (d) EBSD grain boundary map of final pass [33]

While both specimens have lower dislocation densities with respect to the base metal, the sample processed with hot parameter set had the least dislocation density. Moreover, the dislocation density decreased dramatically by consecutive passes, due to the heat provided for annealing and dynamic recrystallization (Figure 2-16).

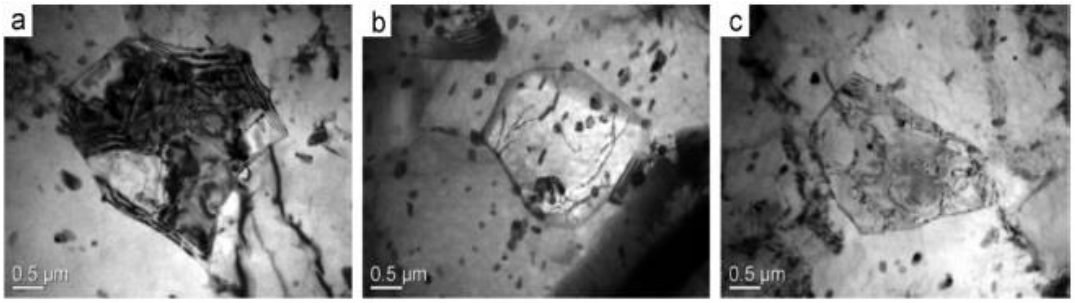

Figure 2-16. The change of dislocation density during the multi-pass FSP (a) First pass, (b) Second pass, (c) Final pass [33]

According to the Humphrey model [34], grain growth may happen in continuous or discontinuous manner. While continuous growth takes place uniformly, in discontinuous growth, abnormal grain growth (AGG) in a portion of the grains occurs. In his model, the mean radius of grains and boundary type (misorientation θ, energy ϒ and mobility M) are considered as the effective variables in growth (Figure 2-17).

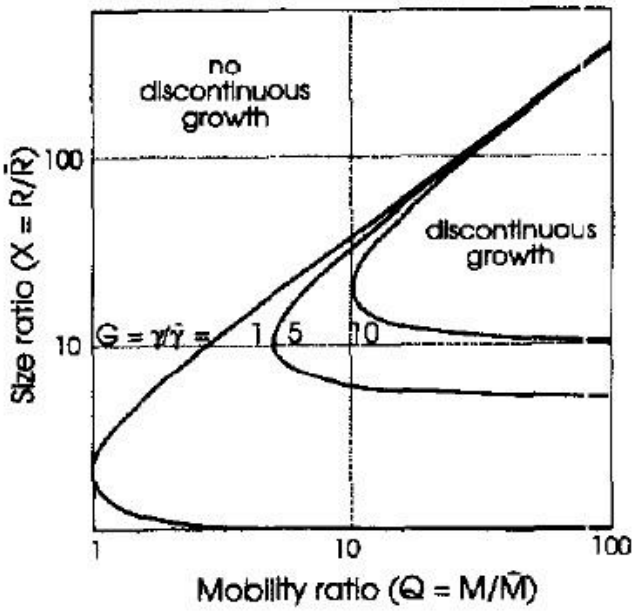

Figure 2-17. Conditions for discontinuous growth as a function of the relative size, boundary energies and mobilities of the grains [34]

As a conclusion of this model, applicable for materials with high stacking fault energy such as aluminum, a scheme for discontinuous growth of a specific grain with respect to average grain size is presented at Figure 2-18.

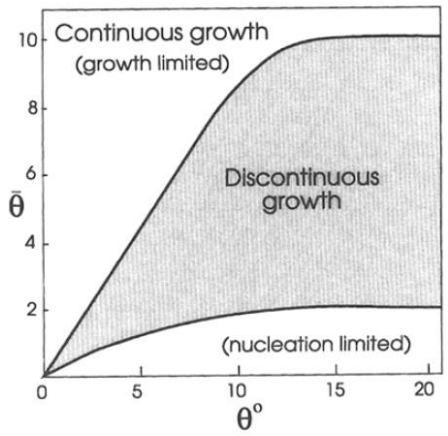

Figure 2-18. Conditions for which discontinuous growth is predicted [34]

Humphreys' second study [35] focuses on effect of second phase particles for grain growth. Adding the dimensionless pinning term, Z.

$Z = \frac{3f_v R}{d}$ in which f_v is fraction of particles with diameter of, d.

In Figure 2-19, the pinning effect of the particles with respect to size ratio of a specific grain is shown. It is seen that with small value of Z, even low size ratios may cause abnormal grain growth.

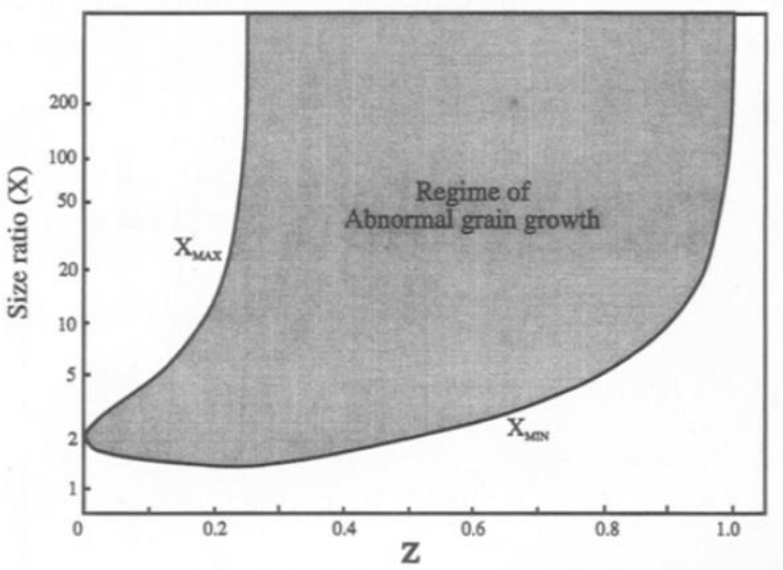

Figure 2-19. The effect of particles on abnormal grain growth of grain with various size ratios [35]

There are a few recent studies on heat treatment of FSW/Ped heat treatable Aluminum alloys [36] [37] [38]. It has been concluded that, at the temperatures above the recrystallization temperature, annealing process results in instability of microstructure and AGG. This issue may seriously affect the superplasticity of nugget zone obtained through fine microstructure.

The stability of microstructure after the FSP is observed to be higher when the hot parameter sets were used [33]. While annealing process (10 minutes at 465°C) of the plates FSPed using the cold parameter set results in a high amount of AGG, the same annealing process leaves the FSPed plates of hot parameter set with only a few coarsened regions (8.1%). The AGG is observed mostly in the roots of the nugget zone. Furthermore, increasing the annealing time from 10 minutes to one hour has increased the AGG region up to 23.3%. Thus, the cold parameter sets are not efficient to keep the stability of the FSPed region when the plate is going to be subjected to elevated temperatures i.e. the heat of the fusion welding. Chen et al. have applied Humphreys'

model [35] to the FSPed Al-5083 plates, and have discovered different grain growth behavior for each of the parameter sets in the nugget zone (Figure 2-20).

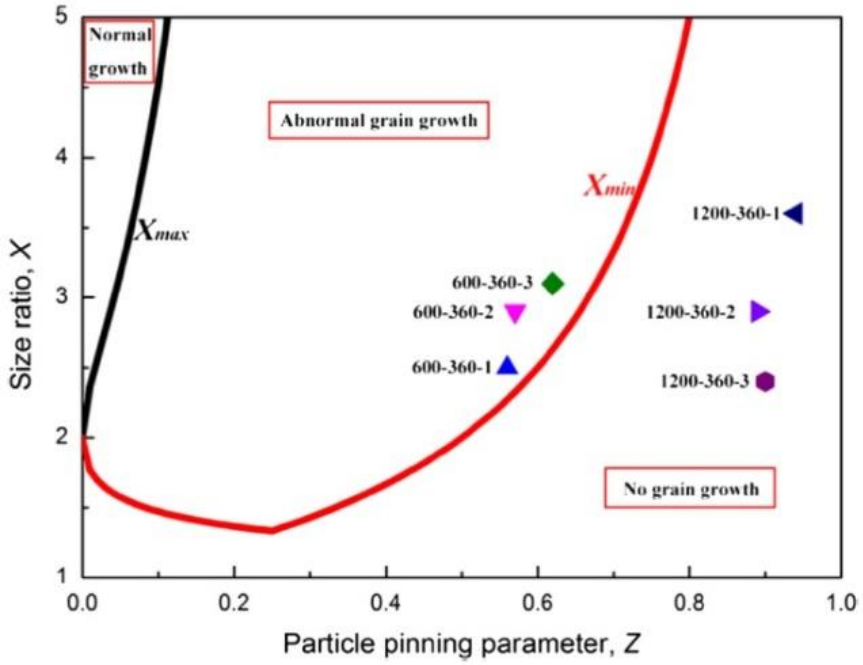

Figure 2-20. Stability prediction based on Humphrey model [33]

CHAPTER 3

EXPERIMENTAL

3.1. Base Metal

20 mm thick 5083-H111 Al-alloy plates (rolled and work hardened) were used. Prior to spectrometry, the samples were ground with 400 grid abrasive papers. Standard and experimental chemical compositions of base metal are given in Table 3.1.

Table 3.1. Chemical analysis of the base metal

5083 H111	**Si**	**Fe**	**Cu**	**Mn**	**Mg**	**Zn**	**Cr**	**Ti**
Experimental	0.17	0.4	0.04	0.56	4.79	0.04	0.09	0.05
Standard	0.4-0.7	0.4*	0.1*	0.4-1	4-4.9	0.25*	0.05-0.25	0.15*

* Maximum Amount

3.2. Methods Used

Conducted Test methods and the Test Equipment:

- Chemical Analysis; Optical Emission Spectrometry (WAS Foundry Spectrometer)
- Micro-structural Evaluation; Polarized Optical Microscopy (Olympus) & Scanning Electron Microscopy (FEI)
- Hardness Test; Micro Hardness Test (Shimadzu Micro Hardness Tester)
- Tensile Test; Uniaxial Tensile Test (Instron Universal Testing Machine)

- Crack Propagation Test; (Servo Hydraulic Machine (MTS), Crack Mouth Opening Displacement Clip on Gage, Mobile Optical Microscope, MATLAB Scripts)

Table 3.2 summarizes the overall methods and tests performed in this study.

Table 3.2. Overview of the experiments

Characterization Method	Base Metal	FSPed Base Metal	GMAW Weldment	GMAW of FSPed Bevel
Chemical Analysis	✓		✓	
Microstructure Investigation	✓	✓	✓	✓
Hardness Test	✓	✓	✓	✓
Tensile Test	✓	✓	✓	✓
Crack Propagation Test	✓	✓	✓	✓
Radiographic Test		✓	✓	✓

3.3. Friction Stir Processing

3.3.1. Operational Procedures

The process was done on plates of 170 mm x 300 mm x 20 mm, with penetration of the pin to the surface of the plates. A volume of 50 mm x 250 mm x 20 mm was FSPed. Depth of the operation was varying according to applied parameter set. Tool

penetration depth was about 11 mm, while applying the optimized parameter set. In order to maintain a processed plate with thickness of 20 mm, both sides of plate had to be processed. Since at each pass only a portion of cross-section area was processed, the overlapping technique was employed, i.e., FSP is performed several times on the plates side by side so that the whole volume is processed. Performing 10 passes at each side of the plate, a volume with width of 45 mm was totally FSP-ed. The cross-sectional macro illustration of overlapping passes is demonstrated in Figure 3-1. The overlapping was done symmetrically for both of the rolling surfaces. The probable defects were mostly observed at the advancing side. Therefore, overlapping were conducted, considering this fact. The first pass was initiated from one side and since the rotational direction was only allowed in counter clock-wise direction, it had to travel in such a direction which the next pass will overlap with its advancing side. Selection of overlapping direction eliminated the possible defects of the advancing sides. This process was continued until the tenth pass.

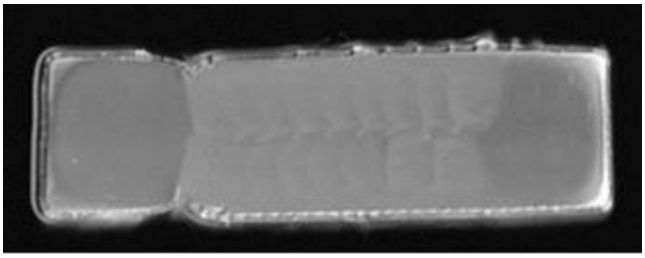

Figure 3-1. Macrograph of the FSPed plate with the overlapping technique

3.3.2. Selection of FSP tool and Optimization of Process Parameters

In order to decide the most appropriate tool, three FSP tools were tried; A01, Triflude and Triflat (Figure 3-2). Furthermore, in order to decide the optimum FSP parameter set, trial and error was applied. First, considering the available facilities, some variables were fixed. Secondly, variations on rotational and travelling speed of the tool were studied. After a few trials with variations in tilt angle, it was decided to be fixed at 0°.

The tool used for FSP had a length of 9mm and 9mm upper diameter. The shoulder diameter of the tool was 20 mm. Fixing the parameter set and the tool design, overlapping trials were conducted.

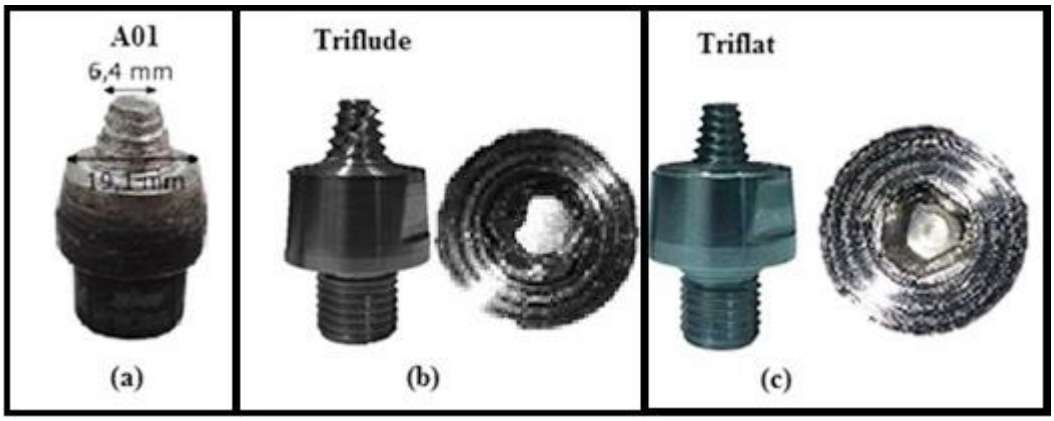

Figure 3-2. Photographs of the tools used in the experiments

3.3.3. Measurement of Temperature

To investigate the change of heat input by FSP with respect to change of parameters, temperature was measured during the FSP trials. The K-type thermocouples were placed in 4 different spots. These thermo-couples were buried inside the plates in a way that pin touches them on its traveling path. Data was taken with SCXI-1112 module of National Instruments with a frequency of 20Hz to detect sudden temperature changes.

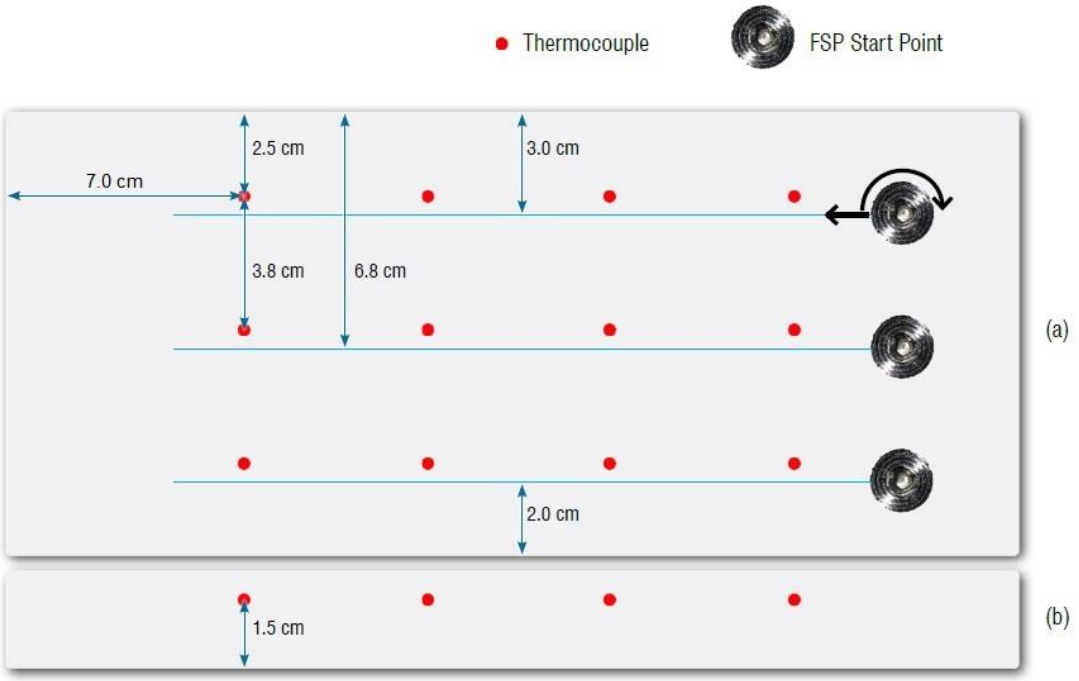

Figure 3-3. Positions of the thermocouples (a) Top view, (b) Side view

3.4. Gas Metal Arc Welding

Direction of welding was chosen to be parallel to the rolling direction. AWS ER5356 rods of 1.2 mm diameter were used as the filler material. Welding-grade argon as the shielding gas with at least 99.998% purity was used. The plates were beveled from both sides to form a double-V groove (Figure 3-4). The welding parameters are given in Table 3.3. The same parameters and material were used for both base metal plates and FSPed plates. Plenty of trials were performed to find the appropriate parameter.

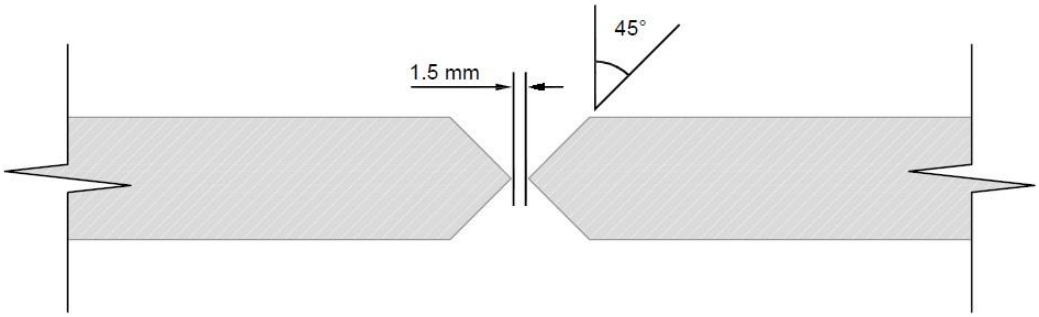

Figure 3-4. Bevel geometry for GMAW

Table 3.3. Process parameters of GMAW

	Wire Feed Rate (m/min)	**Arc Voltage (V)**	**Average Welding Current (A)**	**Average Linear Welding Speed (mm/s)**	**Gas Flow Rate (lt/min)**	**Average Heat Input (kJ/mm)**
Root pass	10.5	22.5	170	5.3	18	0.5
Filler passes	12	25	185	5.7	18	0.6

3.4.1. Welding of Friction Stir Processed Plates

The FSPed plates were cut from the middle such that two plates with the FSP-ed edges are beveled in the same manner for subsequent GMAW process. The macro graph is illustrated in Figure 3-5.

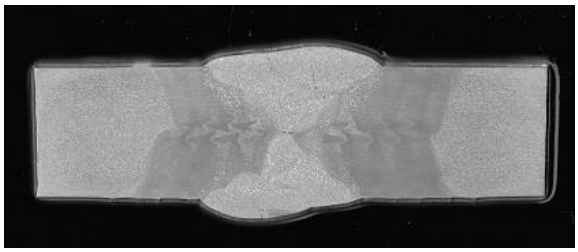

Figure 3-5. Macrograph of the joint (FSPed and welded)

3.5. Radiographic Testing

The radiographic tests were done according to EN ISO 17636-1 using Eresco (200kV) and D4 type films. The exposure time was 80 seconds with 80 kV and 4.6 mA. Optical density of the radiographs was in the range of 1.50-2.00.

The radiographic tests were used to evaluate the soundness of FSP and welding. The results were also used in sampling procedures for the mechanical tests.

Figure 3-6. Radiographs (a) welded plates, (b) FSPed plate

The porosities formed during the GMAW process are seen as the black points in Figure 3-6 (a). Radiograph of the FSPed plate, is presented in Figure 3-6 (b).

3.6. Microstructural Analysis

For microstructural analysis, optical microscope (OM), scanning electron microscopy (SEM), EBSD and EDS were used. Prior to investigations, grinding and polishing were carried out. The samples for metallographic examination were ground with grit

numbers of 120, 400, 800 and 1200 abrasives, respectively. Next, polishing were done by 3 and 1 µm size diamond and final polishing was completed with colloidal silica.

The surfaces of the samples were etched electrically for 80-90 seconds with a direct current power supply with potential difference of 20V in Barkers electrolyte solution (195ml H_2O+5ml HB_4F+5ml H_2O_2). For EBSD investigations, Struers Lectropol-5 electrolytic polishing/ etching equipment and the %5 perchloric acid and %95 ethanol solution were used to prepare the samples.

Fracture surfaces of the polished samples were cleaned with alcohol, and then, examined using FEI brand scanning electron microscope. The surfaces of the samples for EDS analysis were prepared by mechanical polishing.

Average grain size was measured according to ASTM E112 by the intercept method.

3.7. Mechanical Testing

3.7.1. Tensile Test

Tensile tests samples were prepared according to ISO 15614-2. The samples from the base metal and multi-pass FSPed base metal were prepared as illustrated in Figure 3-7 (a).

Because of weld defects, HAZ of welded and FSPed welds were tested by creating a curvature of R=112 mm and the narrowest part of specimen was the region of study, where a 2 mm notch was created at each side as illustrated in (Figure 3-7 (b)).

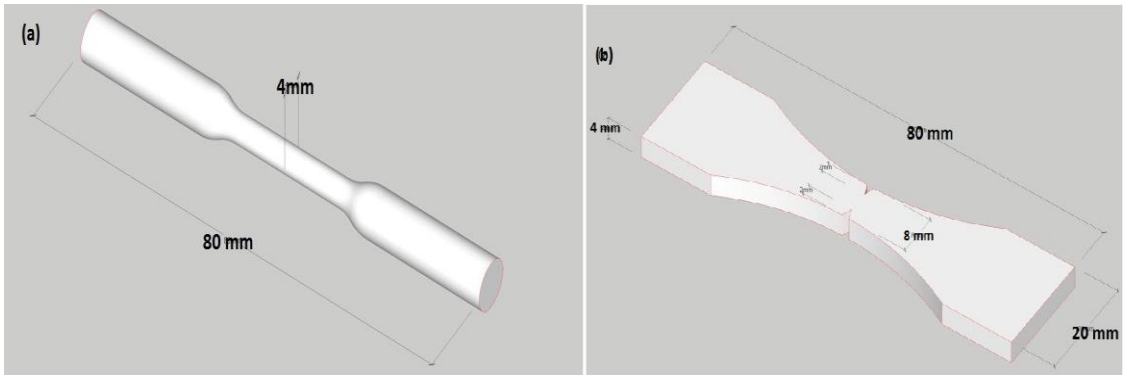

Figure 3-7. Sketch of tensile test specimens
(a) cylindrical specimen, (b) notched specimen

The tensile test specimens were loaded perpendicular to rolling direction. Since, the directions of the welding and FSP were parallel to the rolling direction.

3.7.2. Hardness Test

Measurement loads of 9.807 N and 19.613 N was used for HV1 and HV2 values, respectively. The loading time was 10 seconds. While some measurements were taken randomly on the base metal surface, the other measurements were taken along the lines from base metal through the HAZ to weld metal with specific spacing between each indentation. Then horizontal and vertical hardness profiles were obtained. In order to compare the change of hardness values according to the depth from the surface, hardness profile lines were constructed at 2mm and 7mm below the surface.

3.7.3. Fatigue Crack Propagation Test

The test specimens were prepared according to ASTM E647 (Figure 3-8). Crack initiation and growth measurements were performed at room temperature by means of optical meter and Crack Opening Displacement (COD) transducer. Three samples for the base metal (parallel to the rolling direction), three samples for the HAZ (parallel to the welding direction) and five samples for the HAZ of the FSPed and welded metal

(parallel to welding direction) were prepared. The notches on HAZ specimens were located as shown in Figure 3-9 specified as a white line .The tests were conducted using the parameters given below:

P = 1815 N ± 1485 N (P_{min}=330 N, P_{max}=3300 N), R = 0.1, f = 10 Hz

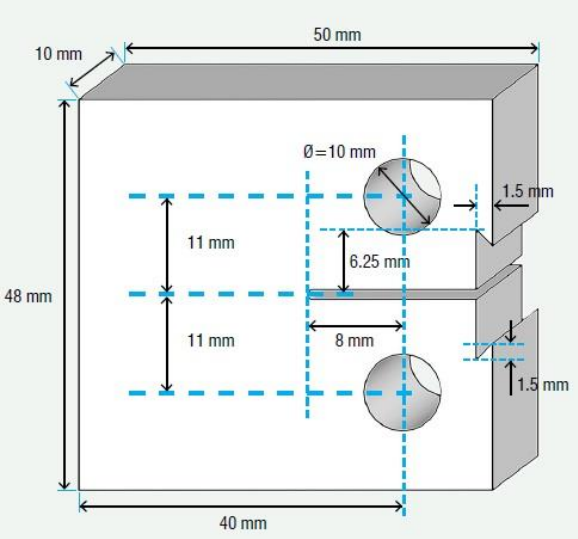

Figure 3-8. Schematic view of the compact tension specimen

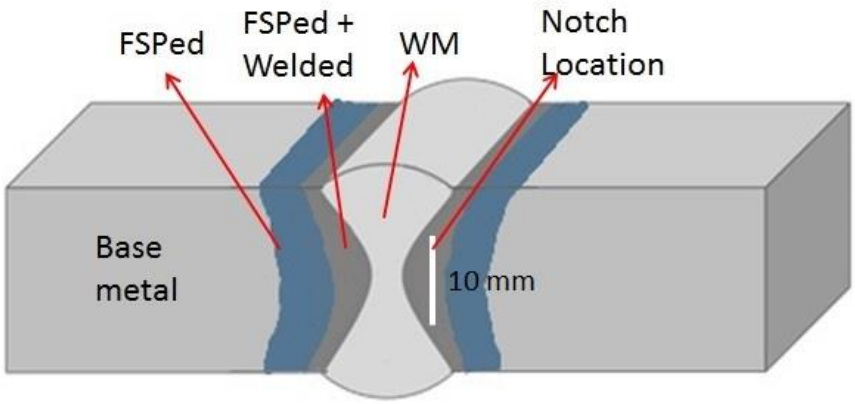

Figure 3-9. Notch location at HAZ for compact tension specimen

Maintaining the pre-crack length, the optical measurement was recorded until the last cycles of crack growth. A portable optical microscope with a precision of $9.10x10^{-3}$ mm was used to measure the crack length.

In order to convert the data received from COD transducer, MATLAB scripts were written. First, the opening displacements were converted to crack sizes specified for each cycle by calculating the slope of P versus V_m graph for that cycle. Six points on P versus V_m graph were recorded for each cycle. The slope for each cycle was converted into crack size utilizing the formula (8) given in ASTM E399, Appendix A4.5.5. Second, using the incremental polynomial method given in ASTM E647 Appendix X1.2, the stress intensity factor (ΔK), versus crack growth rate was plotted. Finally, the constants of Paris-Erdoğan equation were calculated. The second and third processes were repeated for optical data, as well.

$$a/W = (1000 - 4500U + 13157U^2 - 172551U^3 + 879944U^4 - 1514671U^5) \quad (8)$$

where, $U = \frac{1}{1+\sqrt{\frac{E' B_e V_m}{P}}}$

V_m = crack mouth opening displacement, (m),

P = applied force, (N),

B = specimen thickness,

$B_e = (B-B_N)^2/B$,

E' =elastic constraint modulus (Pa) (E for plane stress; $E/(1-\nu^2)$ for plain strain),

ν = Poisson's ratio

For each cycle the crack size was maintained using the MATLAB script. However, because of scattered data for some of the cycles, data elimination process was applied. In this stage, starting from calculation of average of first 41 crack sizes, the value of 21st crack size was considered. The data which deviated more than 0.0005 mm of the average of neighboring 20 values, were eliminated. This process was repeated until the last 20th cycle. Figure 3-10 is an example of data elimination process following the conversion of V_m to a.

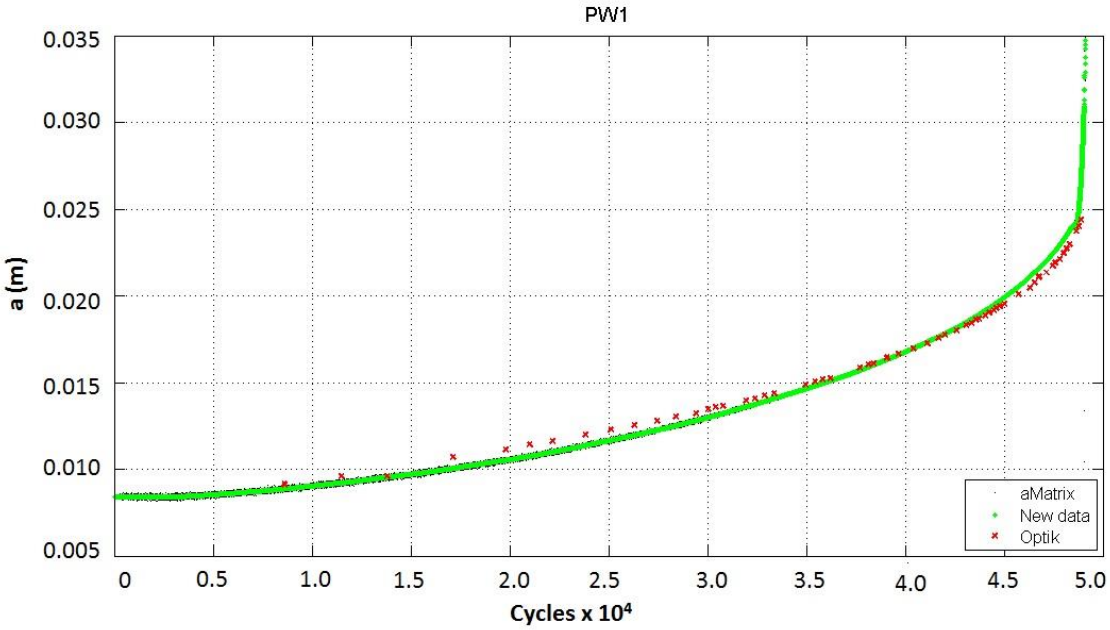

Figure 3-10. Crack size versus number of cycles curve for the HAZ of the FSPed + welded metal after data elimination.

In order to calculate the stress intensity factor range in a given crack growth rate the incremental polynomial method in ASTM E647 was used. The derivative of each polynomial fitted to a data, is equal to crack growth rate. Stress intensity factor range was also found for each given crack size. Incremental polynomial method was applied using a second order polynomial which was fitted to each data together with n neighbors around it. Therefore, this method was applied on each 2n+1 data points. In optical data n was taken as 3. In CMOD data, n was equal to 500.

$$\Delta K = \frac{\Delta P}{B\sqrt{W}} \frac{(2+\alpha)}{(1-\alpha)^{\frac{3}{2}}} (0.886 + 4.64\alpha - 13.32\alpha^2 + 14.72\alpha^3 - 5c.6\alpha^4) \qquad (9)$$

Where $\alpha = a/W$, and this expression is valid for $a/W \geq 0.2$.

The results of these processes for optic and CMOD data are illustrated in Figure 3-11.

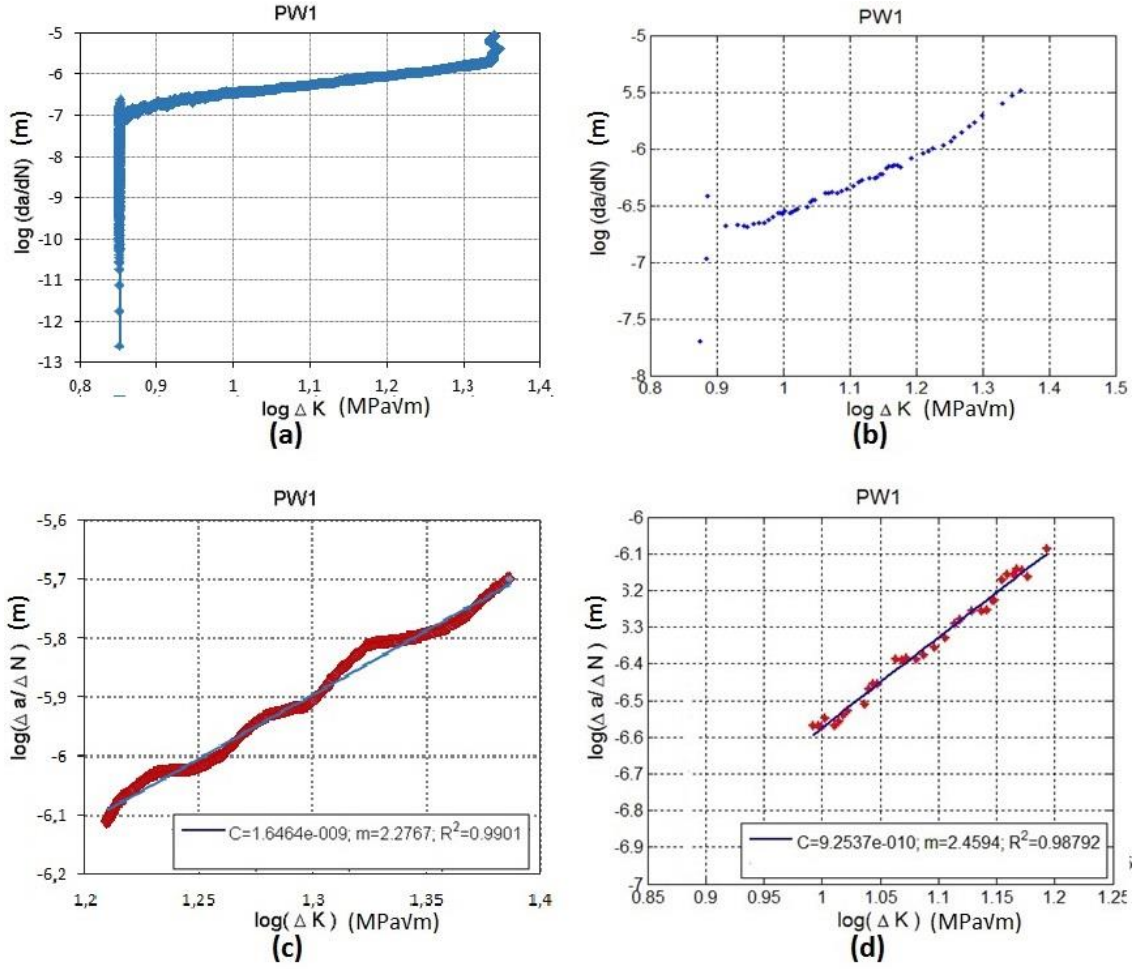

Figure 3-11. log (da/dK) versus log (ΔK) curves of FSPed and welded specimen

(a) Full range CMOD data, (b) Full range optical data,

Best fit line of steady state zone (c) CMOD data, (d) Optical data

CHAPTER 4

RESULTS AND DISCUSSION

4.1. FSP Applications

For friction stir processing, tool geometry, rotational speed, traveling speed, nominal force, material thickness, material temperature and tilt angles are the main variables. In this study the tool geometry, rotational speed, travelling speed and tilt angle were selected as the variable parameters. A series of trials were performed using A01, Triflude and Triflat tools (Figure 3-2). A01 were used mostly for temperature variation measurements, whereas Triflude and Triflat were used for the overlapping processes. The result of the trials showed that Triflat tool gives the best performance for maintaining a continuous and sound pass.

4.1.1. Trials with A01 Tool

Using the department abilities, the A01 tool was designed and manufactured for the first FSP trials. H13 steel was the used material for this tool which is illustrated in Figure 3-2 (a).

Since, during the FSP, plates are subjected to large amount of forces, they had to be fixed firmly before the process. Therefore, after finalizing the fixing process, FSP trials with the parameters illustrated in Table 4.1 were performed. For the sake of saving material, three passes were applied to each plate. The sizing of plates was 30x17x2cm. The travelling direction of the tool was parallel to the rolling direction. The top views of the FSPed plates are given in Figure 4-1.

Table 4.1. FSP parameters conducted with A01 tool

Test Number	Rotational Speed (rpm)	Travelling Speed (cm/minute)	1st Tilt Angle x°	2nd Tilt angle y°	Temperature (°C)	Reached Temperature (°C)
DN1	900	2.1	-	-	446	474
DN2	900	2.1	2	-	459	480
DN3	900	2.1	2	2	454	485
DN4	1120	1.7	-2	-2	425	459
DN5	1400	1.7	2	2	424	458
DN6	560	1.7	2	2	410	426
DN7	560	2.1	2	2	413	422
DN8	560	2.7	2	2	419	467
DN9	355	4.3	2	-2	341	360
DN10	355	6.8	2	-3	368	397
DN11	355	2.1	2	2	432	457
DN12	355	4.3	2	-3	313	336
DN13	224	4.3	2.5	-2	351	367

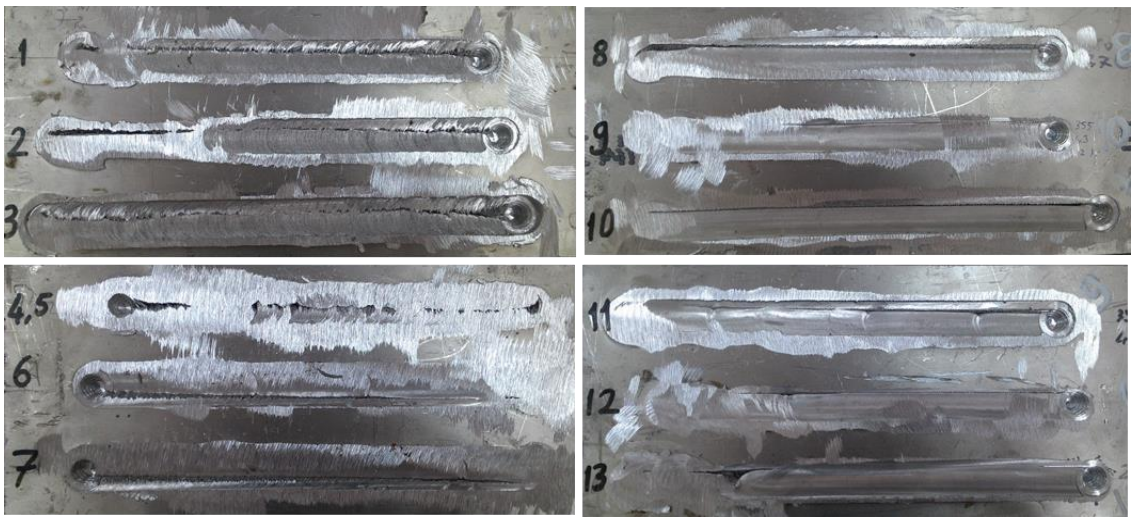

Figure 4-1. Top view of the plates FSPed with A01 tool

In the first experiment set, the rotational speed was the variable (355, 560 and 900 rpm) while the travelling speed was fixed to 2.1 cm/min. Figure 4-2 shows that, as the rotational speed increases, the maximum temperature increases due to the heat input created by frictional forces. In the second experiment set, the rotational speed was fixed to 355 rpm, and the maximum temperatures were measured at three different travelling speeds (2.1, 4.3, 6.8 cm/min). Figure 4-3 shows that, the decrease in travelling speed causes the increase of FSP temperature. Since the plate is subjected to the frictional forces for a longer period in lower travelling speed, the temperature can increase further.

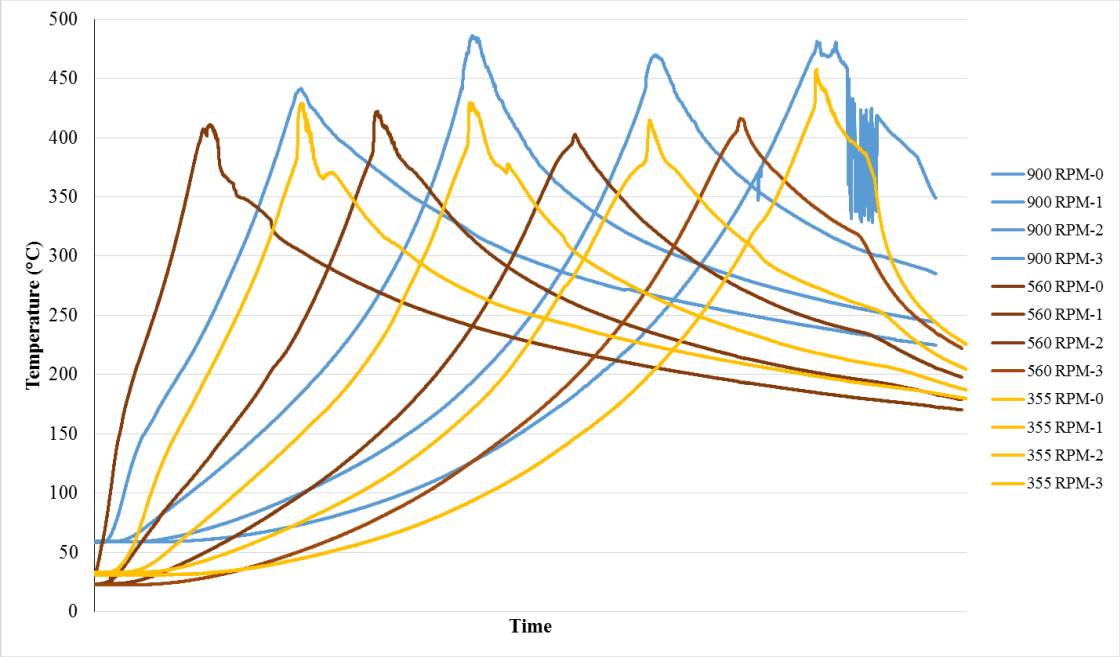

Figure 4-2. Effect of rotational speed of FSP on the maximum temperature, measured in the sample (traveling speed = 2.1 cm/min)

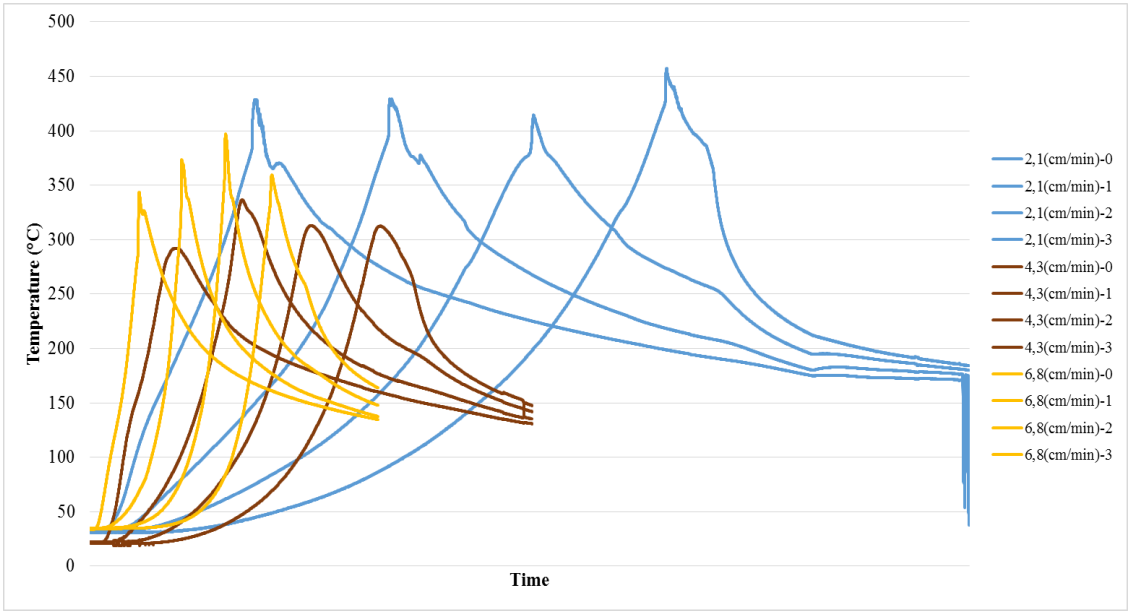

Figure 4-3. Effect of travelling speed of FSP on the maximum temperature measured in the samples (rotational speed = 355 rpm)

In Figure 4-4 these phenomena are even more obvious by comparing two extreme conditions at each experiment.

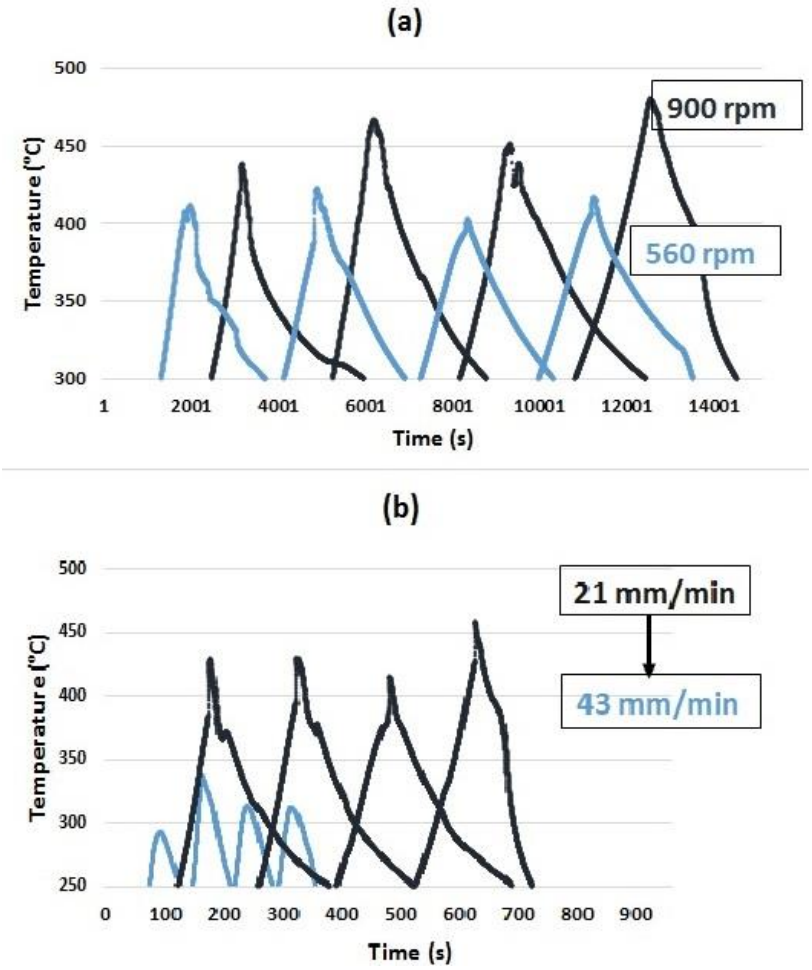

Figure 4-4. Variation of temperature:
(a) constant travel speed, (b) constant rotational speed

To sum up, during the first trials the continuity of the FSPed material could not be maintained because of the insufficient tool design. However, invaluable data was maintained by studying the temperature variations. These data were utilized to explain the grain structure of the specimens FSPed by other tools. In Figure 4-5, the radiographs and macrographs of the FSPed plates are displayed.

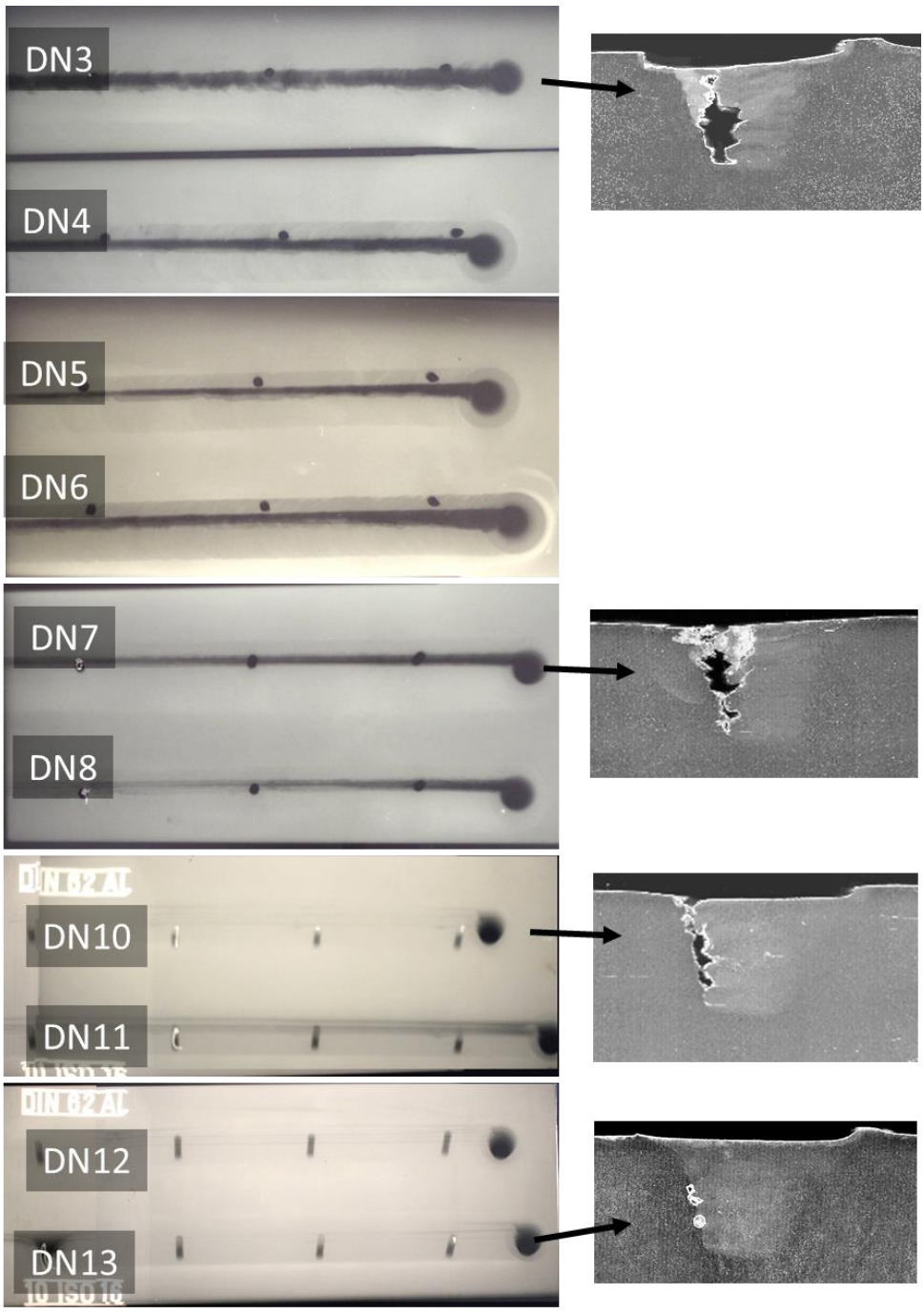

Figure 4-5. Radiographs and side views of the single pass FSPed plates

4.1.2. Trials with Triflute Tool

Because of the helical threads of the Triflute tool, the only possible rotation was counter clock-wise. This creates a material flow towards the bottom layers of the passes. Handful of trials were made with Triflute tools after they were delivered. However, their delicate structure didn't handle the loads applied on them during some if the extreme parameters. Due to the failures in the pin of the tools during trials, it was decided to not consider them as the main tool for the FSP applications. The parameters used in the trials are given in Table 4.2. The FSP passes with Triflute tool, were sound for most of the parameters.

Table 4.2. Parameter set performed with Triflute Tool

Trial Number	Rotational Speed (rpm)	Travelling Speed (mm/minute)
N19	210	285
N20	210	185
N21	110	185
N22	150	185
N23	980	40
N24*)	720	-
N25*)	530	-
N26	530	65
N27	530	100
N28	530	185
N29	390	65
N30	390	100
N31	210	285

4.1.3. Trials with Triflat Tool

Following adequate number of trials with two previous tools, the optimized parameters were almost clear. First experiments with Triflat tool is listed in Table 4.3. Obtaining those results, two feasible (in terms of soundness and limits of the machining device) extreme parameters, as the upper and lower parameters from temperature point of view were applied. Exceeding these limits would end up to discontinuities in the passes. Therefore, a hot and a cold pass were applied on a plate in order to examination and comparison of the microstructures. The plate is exhibited in Figure 4-6.

Table 4.3 Parameter sets performed by Truncated 3-f Tool

Test Number	Rotational Speed (rpm)	Travelling Speed (mm/min.)
N32	210	185
N33	530	185
N34	530	100
N35	720	65
N36	720	100
N37	290	100

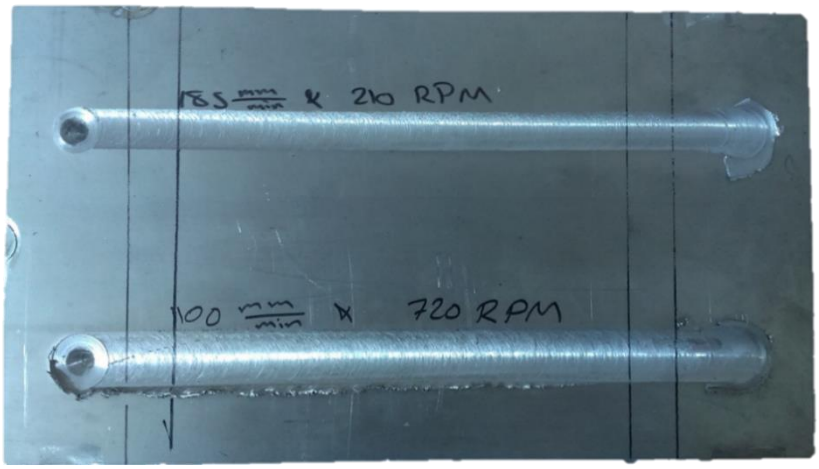

Figure 4-6. Top View of the plate on which the cold and hot parameter sets were applied

As it is observable from Figure 4-6 and Figure 4-7, the hot parameter (720 rpm, 100 mm/min.) was obtainable by more penetration of the tool pin. Because of the high heat input of the hot parameter, softening of the FSPed region is observed to be more than that of cold parameter. That's why more axial forces (more penetration) of the tool is needed to maintain a sound pass. These two sets of parameter (720 rpm-100 mm/min. and 290 rpm-185 mm/min.), were then used for overlapping experiment by multi passing. The two overlapped FSP samples are shown in Figure 4-7.

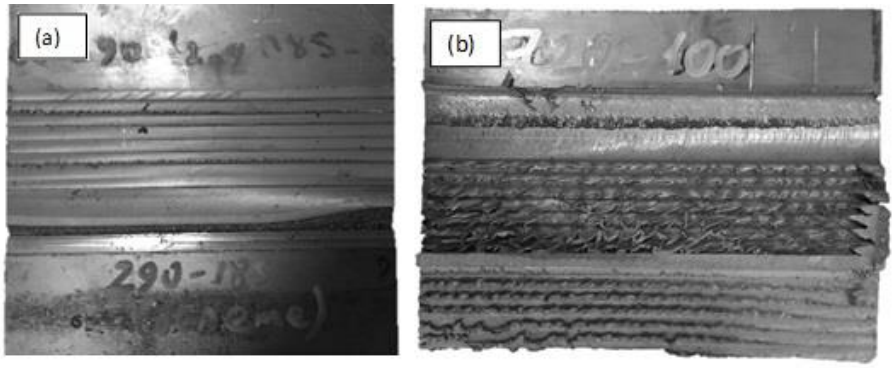

Figure 4-7. Top view of the plates FSPed with the overlapping technique (a) cold parameter set, (b) hot parameter set

Finally, the optimum parameter set was decided as 290 rpm-100 mm/min. Subsequent overlapping processes were conducted using this parameter set.

4.2. Microstructural Analysis

4.2.1. Base Metal

The microstructures of the base metal for three perpendicular directions are shown in Figure 4-8. The effect of rolling can be easily seen from the grain orientation of the grains.

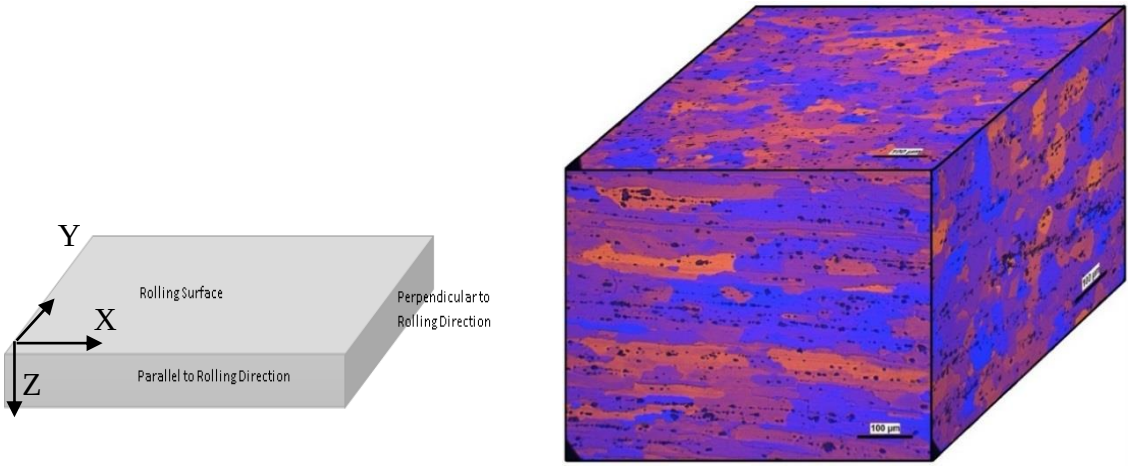

(a) (b)

Figure 4-8. (a) Macro 3-D view of base metal plate,
(b) 3-D Optical microstructural view of base metal

The average grain size of the base metal on the XY, XZ and YZ surfaces were determined as 58, 92 and 25 μm with the maximum standard deviation of 6 μm.

Intermetallic particles of two kinds exist (Figure 4-9). The area fraction of particles on the XY, XZ and YZ planes were measured as 0.4, 0.6 and 0.4 for the black particles and 1.4, 1.2 and 1.4 for the grey particles.

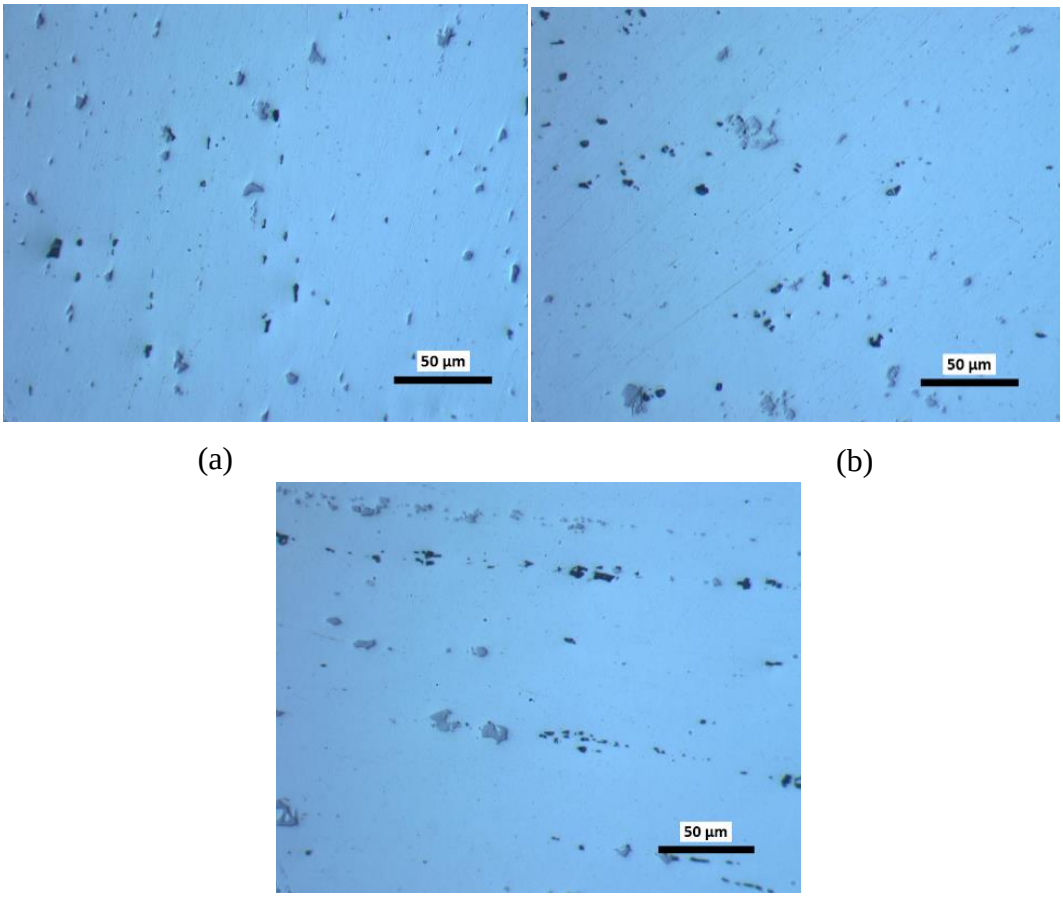

(a) (b)

(c)

Figure 4-9. Optical view of the polished specimens

(a) Perpendicular to the rolling direction, (b) Rolling surface,

(c) Parallel to the rolling direction.

The results of energy dispersive X-ray spectroscopy reveal the difference between the black and grey colored intermetallics. As illustrated in Figure 4-10, the black particles contain Al, Mg and Si whereas the grey ones contain Al, Si, Mn and Fe.

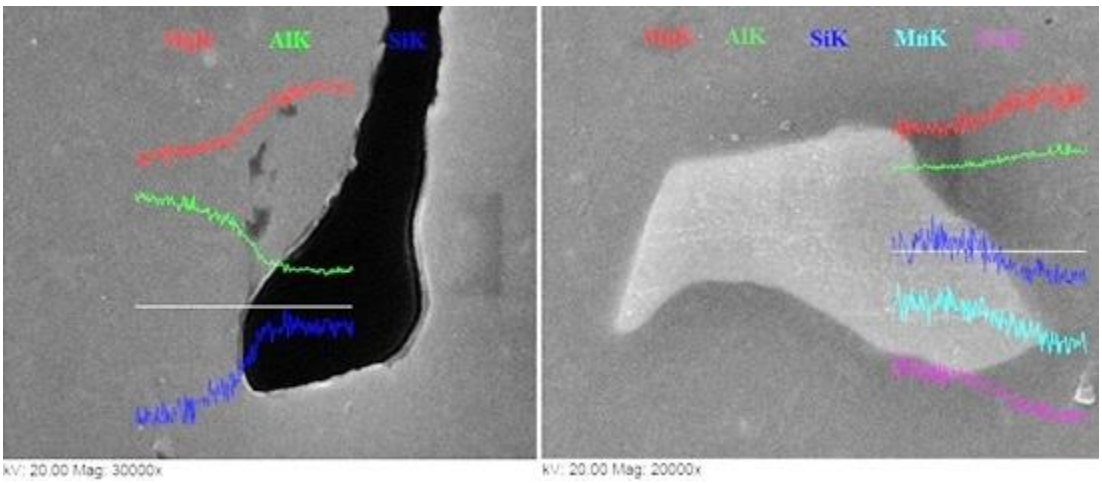

Figure 4-10. EDS results of the intermetallic particles

4.2.2. Friction Stir Processed Metal

Microstructure investigations on FSDed plates indicated differences among the hot parameter and cold parameter sets and the top and bottom parts (Figure 4-11, Figure 4-12). The hot parameter set resulted in coarser grain sizes. The average grain size of the sample FSPed using the hot parameters set is 6±1 μm, while that of sample FSPed using the cold parameter set is 1 μm. For both sets, the grains became coarser it is approached to the plate surface.

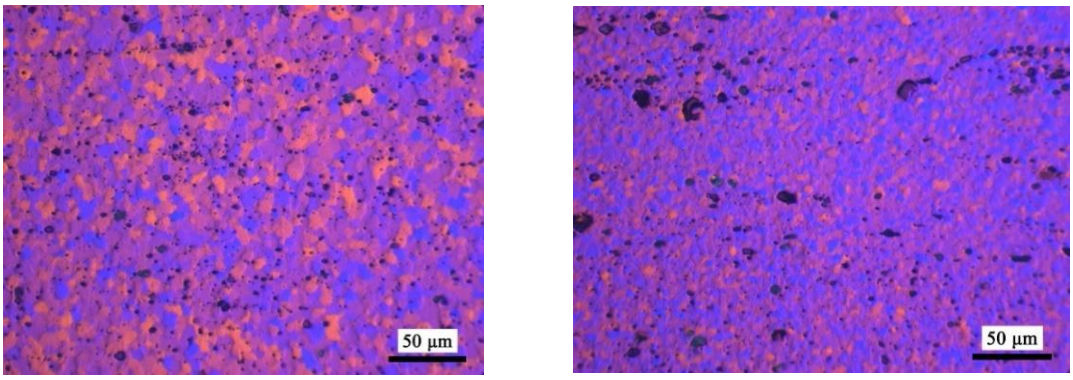

(a) (b)

Figure 4-11. Microstructures after FSP by the hot parameter set

(a) near the plate surface, (b) near the plate center

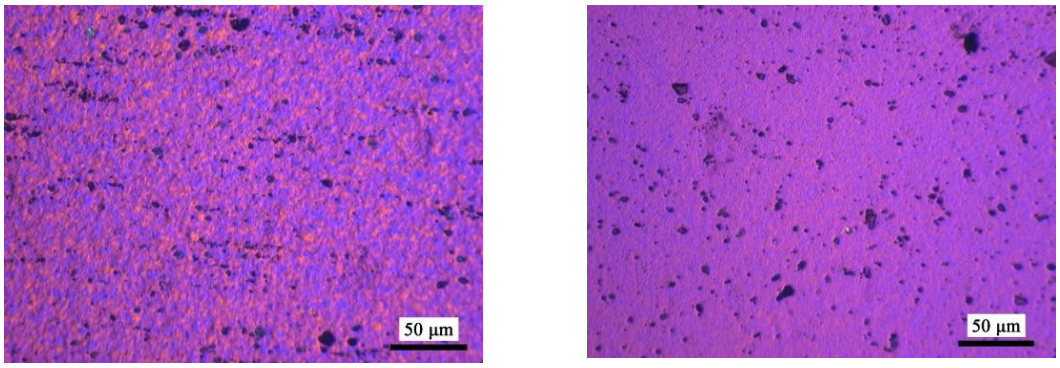

(a) (b)

Figure 4-12. Microstructures after FSP by the cold parameter set
(a) near the plate surface, (b) neat the plate center

The differences in the microstructure can be explained by recrystallization phenomenon. First, higher rotational speed, and therefore, higher heat input of the hot parameter set associates the further growth of the grains. Second, the lower travelling speed of the tool, provides the grains longer time spent at elevated temperatures which assists the grain growth.

Downward material flow, created by the threads on the pin, provides more amount of mechanical work towards the below layers of the FSPed zone and leaves material with higher amount of strains and tangles which somehow complicates the recrystallization process and creates more obstacles for grain growth. This is the reason for smaller grains at the bottom levels of the FSPed zone.

The difference between two advancing and retreating sides of FSPed cross-section was also investigated. The magnifications of two marked regions in Figure 4-13, are shown in Figure 4-14 (a) and (b), respectively from left to right. It is well observed that, while there is a sudden passage from TMAZ to nugget zone in advancing side, this passage is smoother in retreating side.

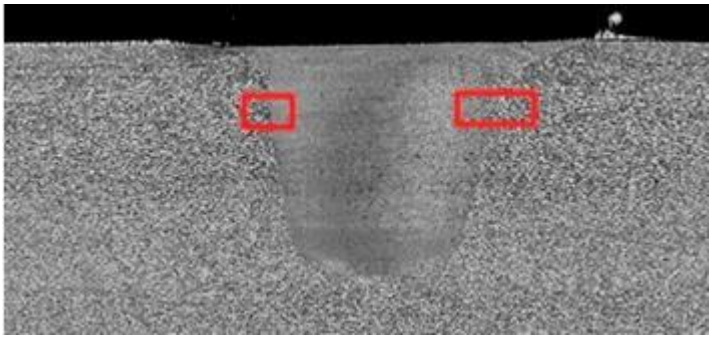

Figure 4-13. Cross-sectional view of the FSPed plate

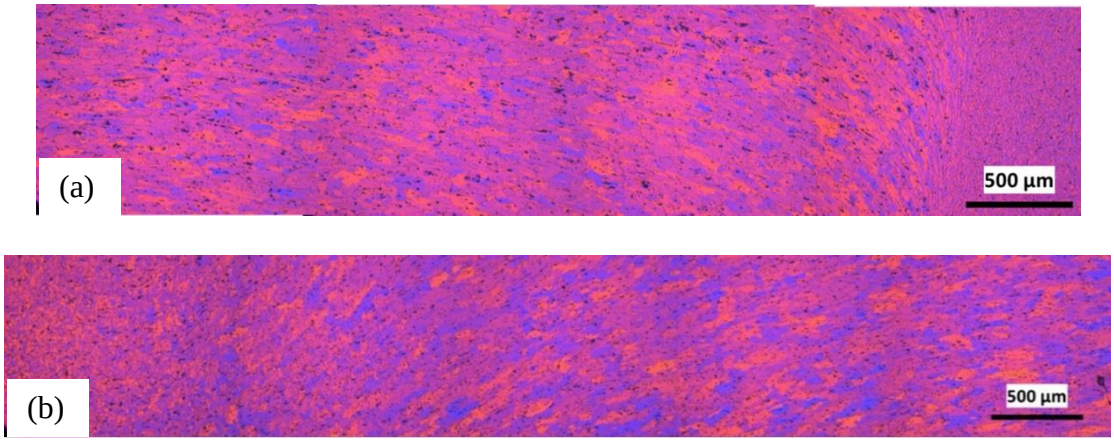

Figure 4-14. The extended microstructural view of passage from neighboring metal to the FSPed region (a) Advancing side, (b) Retreating side

Finally, the effect of the FSP-line overlapping on grain size was studied. While the grain size during hot parameter set was unchanged after over 10 overlapping processes, a grain size coarsening was observed in first passes of overlapping during cold parameter set. Being subjected to heat input of the following passes, grains formed in the first passes were coarsened to 3±1 µm from 1 µm. However, the FSPed plates with hot parameters were not sensitive to the heat of the following passes as plates FSPed by cold parameters were. This may be explained by insufficiency of the heat input for further growth. Chen et al. [33] did not recorded a considerable growth in nugget zone

of hot parameter of their study. They stated, cold parameters are more prone to growth with subsequent heat treatment. Therefore, it may be stated that the growth of the grains is limited in the temperature range which FSP is capable to elevate.

The radiograph of the plate having overlapped FSP lines is presented in Figure 4-15.

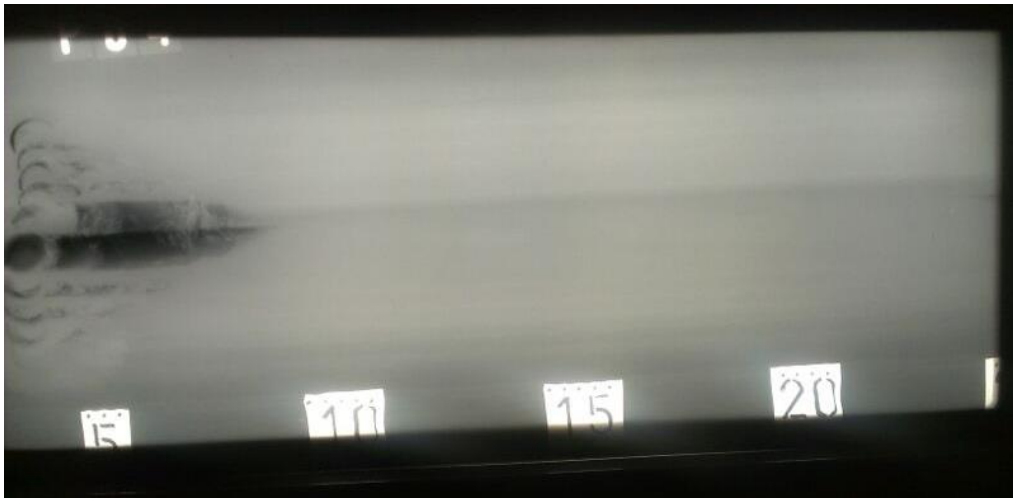

Figure 4-15. Radiograph of the plate having overlapped FSP lines
(290 rpm, 100 mm/min)

In Figure 4-16, electron backscatter diffraction (EBSD) image of the overlapped plate is illustrated. The image is taken from side which has FSPed first.

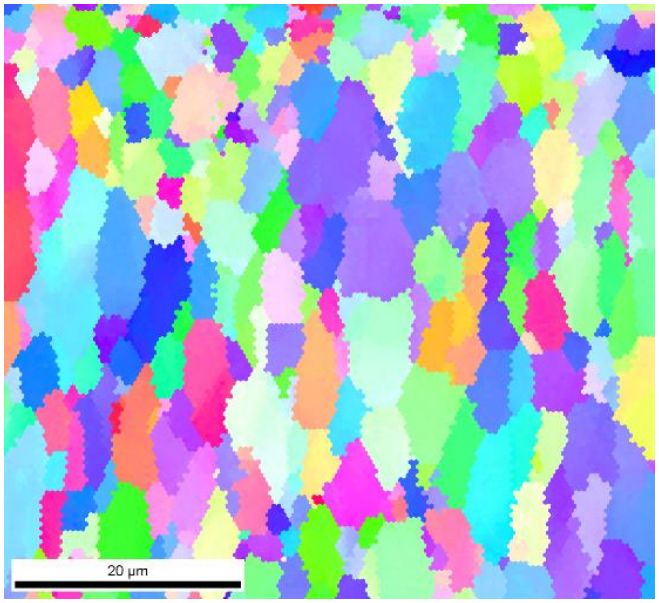

Figure 4-16. EBSD image of the plate after application of the overlapped FSP (290rpm, 100mm/min)

4.2.2. Heat Affected Zone of Base Metal

The macro image of the as-welded base metal is presented in Figure 4-17.

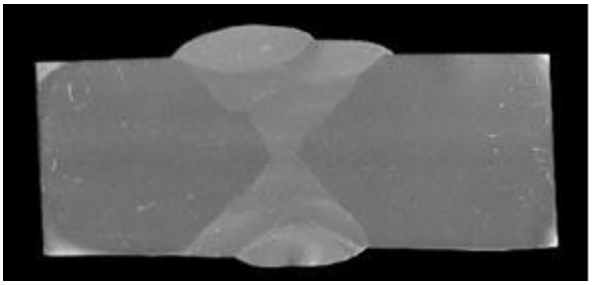

Figure 4-17. Macro view of the welded plate

The extended microstructure view of welded specimen starting from weld metal at left, through the fusion line, HAZ and base metal at right, is shown in Figure 4-18.

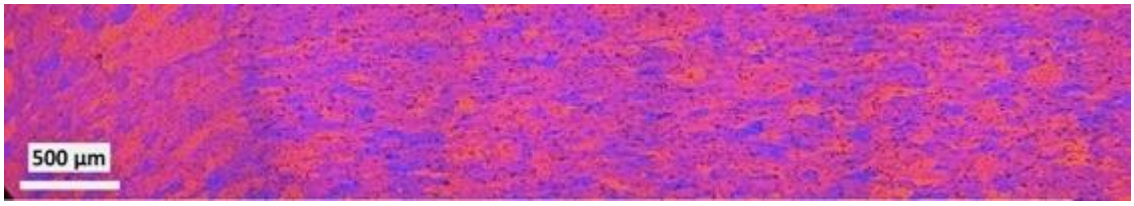

Figure 4-18 Extended microstructure view of the welded plate

A more detailed view of HAZ is also illustrated in Figure 4-19. Because of high heat input, growth of the grains is observable in HAZ region.

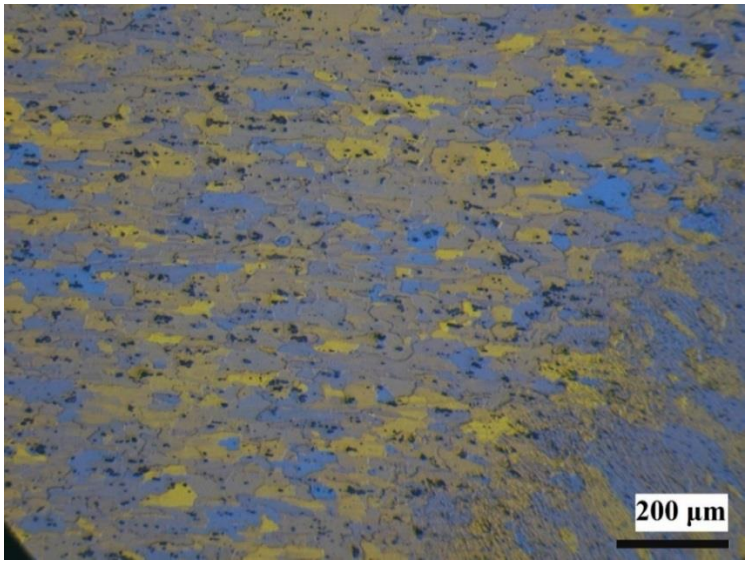

Figure 4-19. Micrograph of HAZ (50x)

H111 tempered alloys are not subjected to high amounts of strain hardening. Although a significant grain coarsening is observed in the HAZ of base metal, existence of more work hardening and therefore, more strain energy, would result in more growth in HAZ.

4.2.3. Heat Affected Zone of the FSPed and Welded Metal

Following the FSP, the beveled plates were butt welded. The macro view of the specimen is presented in Figure 4-20.

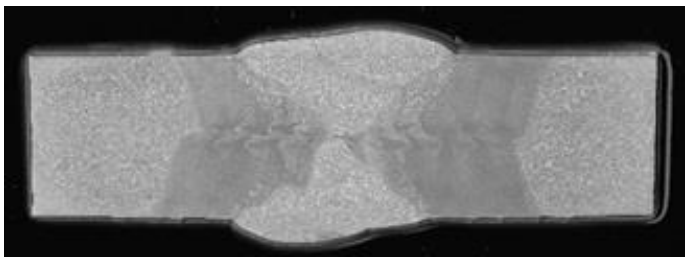

Figure 4-20. Cross-sectional view of FSPed + welded plates

Considering the Figure 4-21, a wide view of weld metal and HAZ vicinity will reveal the fine microstructure of the HAZ region after the welding. There is a slight grain growth next to the fusion line. Average grain size in the HAZ of FSPed and welded plates are measured to be 6 μm. This value is excessively smaller than HAZ of the base metal. However, extra growth is more obvious at specific regions as the distance from fusion line is increased.

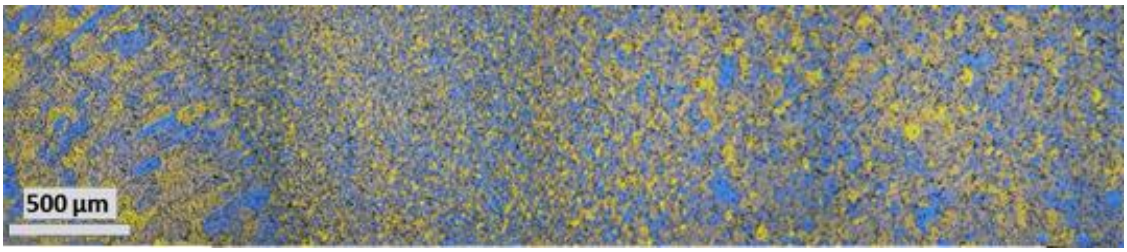

Figure 4-21. Extended microstructure view of the FSPed and welded plates

While the general view of the HAZ microstructure is similar to the Figure 4-22 (a), in some random regions, abnormal grain growth phenomenon was observed, as shown in Figure 4-22 (b). Although discontinuous growth for some grains were recorded up to 30 μm, this behavior was not observed for other neighboring grains. Since the FSPed structure was subjected to excessive amount of heat via welding process, AGG was inevitable despite of pinning effect of secondary particles. Discontinuous growth is known to happen when a few grains overwhelm the Zener pinning effect and consume the neighboring fine grains pinned by Zener drag, while the rest of the grains are essentially stable [39].

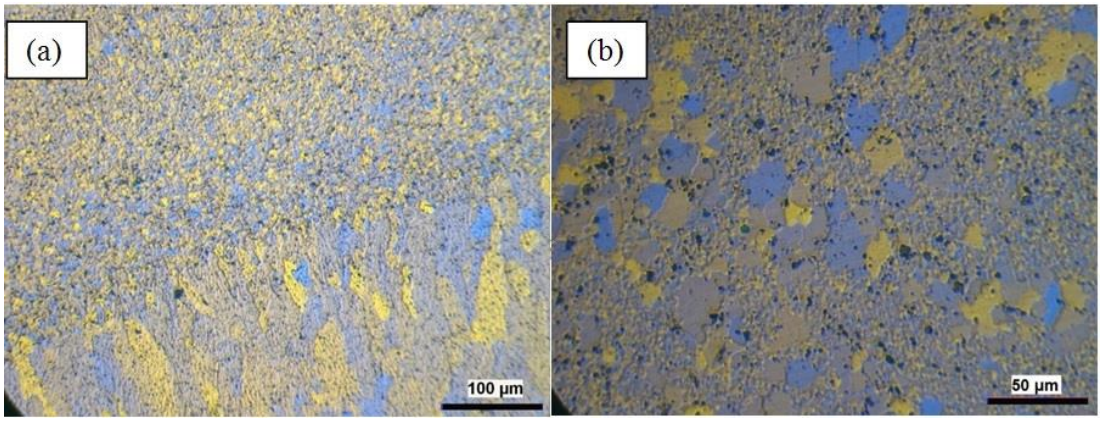

Figure 4-22. Micrographs of HAZ of the FSPed + welded region
(a) Adjacent to the fusion line, (b) HAZ

However, providing more heat to the FSPed region during the GMAW could result in coarsening of the finer neighbor grains, as well [40].

According to model of Humphreys [34], abnormal grain growth (AGG) is an expected formation for the grain boundaries with misorientation between 5° and 10°. These grains are instable which may get affected by any kind of heat treatment after FSP. Works of Chen et al. [33], also admits that AGG takes place at roots of the nugget zone during the annealing process after FSP. Also in previous works it has been observed that, the FSPed region is not uniform in terms of microstructural properties which are important criteria for growth. For instance, he values of stress concentration and residual stresses are found to be greater in advancing side of the nugget zone [41].

Non-uniformity of the grains in FSPed zone is due to heat input of the GMAW. The misoreintation angles of the grains that are seen in Figure 4-16 is given in Figure 4-23. The fraction of grains within the misorientation range of 5°-10° is about 3% of the all grains. AGG is expected to occur for these grains.

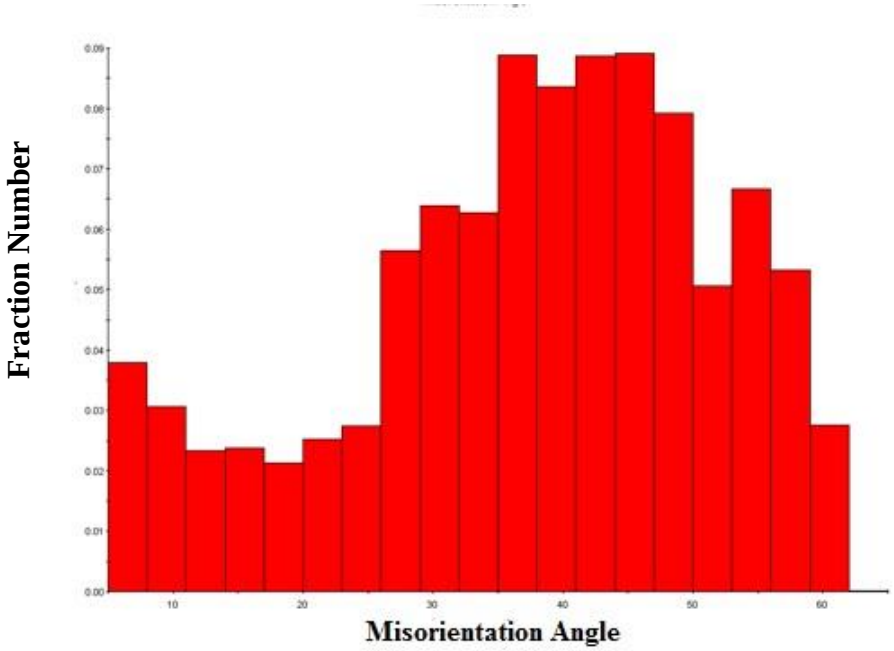

Figure 4-23. The fractions of misorientation angle among grains of overlapped FSPed plate, prior to welding process

However, the fine microstructure was preserved for the majority of the grains. Therefore, significant effects are not expected in the mechanical properties of the FSPed and welded HAZ, compared to FSPed plates.

In order to notice the difference between HAZ of base metal and HAZ of FSPed and welded metal CT specimens, polished and etched surface of the CT specimens, is provided in Figure 4-24. The route of crack propagation is extremely different among two specimens from morphological point of view.

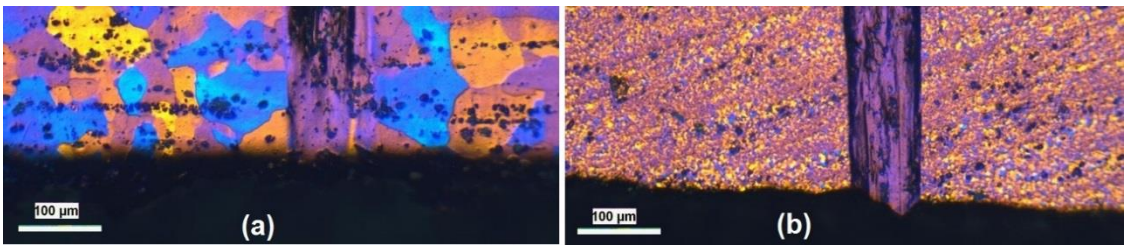

Figure 4-24. A comparison of the HAZ in CT specimens:
(a) The base metal, (b) The FSPed metal

4.3. Mechanical Tests

4.3.1. Hardness Test

The hardness values of the base metal are given in Table 4.4. Higher hardness values were expected at the surfaces which have been subjected to strain hardening. This validates the results maintained from the hardness values of the base metal.

Table 4.4 Hardness values of the base metal

BM	**Surface Perpendicular to the Rolling Direction HV1**	**Surface Parallel to the Rolling Direction HV1**	**Rolling Surface HV1**
#1	91.4	95.3	85.7
#2	91.3	101.0	89.8
#3	94.6	92.0	89.4
#4	97.1	93.0	89.0
#5	94.7	94.7	85.3
#6	91.9	90.5	90.2
#7	91.0	94.0	90.0
#8	93.6	90.3	88.3
#9	89.2	91.9	90.9
#10	93.1	91.1	87.0
Average	92.8±2.2	92.9±3.0	88.6±1.8

4.3.1.1. Hardness of the Base Metal after Friction Stir Processing

The hardness profiles for the two extreme FSP parameters (i.e. 720 rpm – 100 mm/min, and 290 rpm – 185 mm/min) are illustrated in Figure 4-25 and Figure 4-26. The most effective phenomena of the parameters on the hardness is the heat input. Since the heat input is in direct relation with parameter with higher RPM/speed, the hardness of specimens processed under 720 RPM – 100 mm/min differed dramatically with respect to the colder parameter.

Hardness values are taken both in horizontal and vertical directions. In the vertical direction, hardness increases towards the center because of the microstructural differences between top and bottom of the nugget zone. In the horizontal direction, the order of overlapping is more significant for hardness. Since every pass of FSP acts as a heat treatment, the hardness after the first pass is lower than that after the last pass.

The average of vertical and horizontal hardness values for the parameter of 720 RPM – 100 mm/min was measured to be 88±2 HV2 and for the parameter of 290 RPM -185 mm/min was measured as 92±4 HV2.

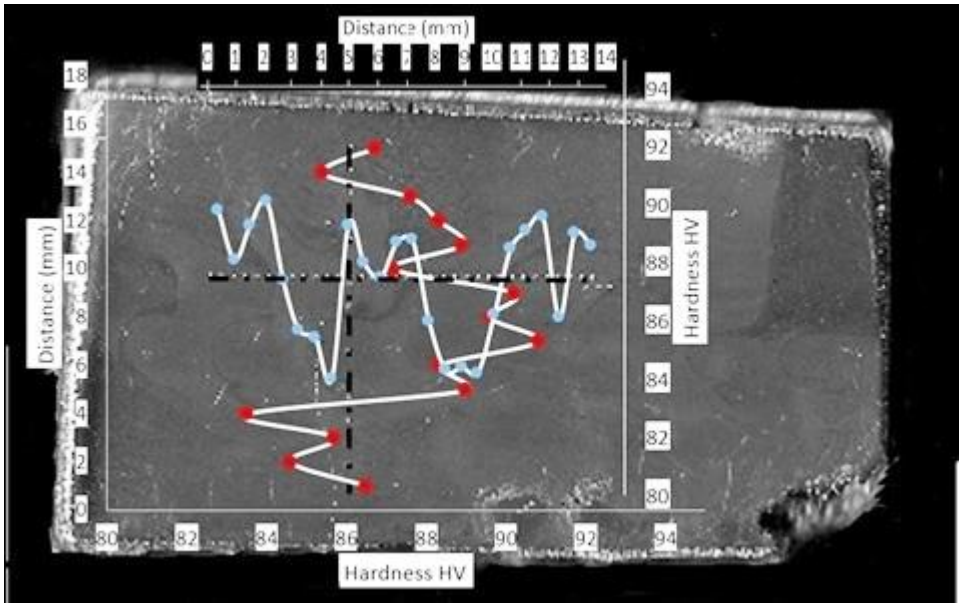

Figure 4-25. Vertical and horizontal hardness profiles of the sample FSPed with the overlapping technique (720 RPM – 100 mm/min)

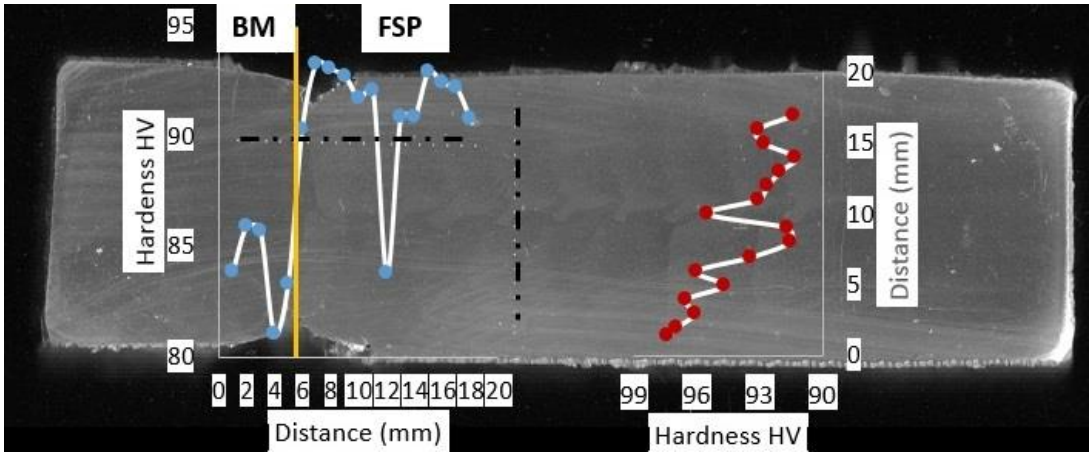

Figure 4-26. Vertical and horizontal hardness profiles of the sample FSPed with the overlapping technique (290 RPM – 185 mm/min)

In Figure 4-27-a, the difference among morphology of retreating side and advancing side is shown by hardness values. Because of the higher amount of strain hardening in advancing side higher hardness values is obtained. This phenomenon is not obvious in

Figure 4-27 (b), because of the higher heat input of the process and relatively softening of the material, subsequently. However, this heat input results in formation of heat affected zone adjacent to the overlapped nugget zone.

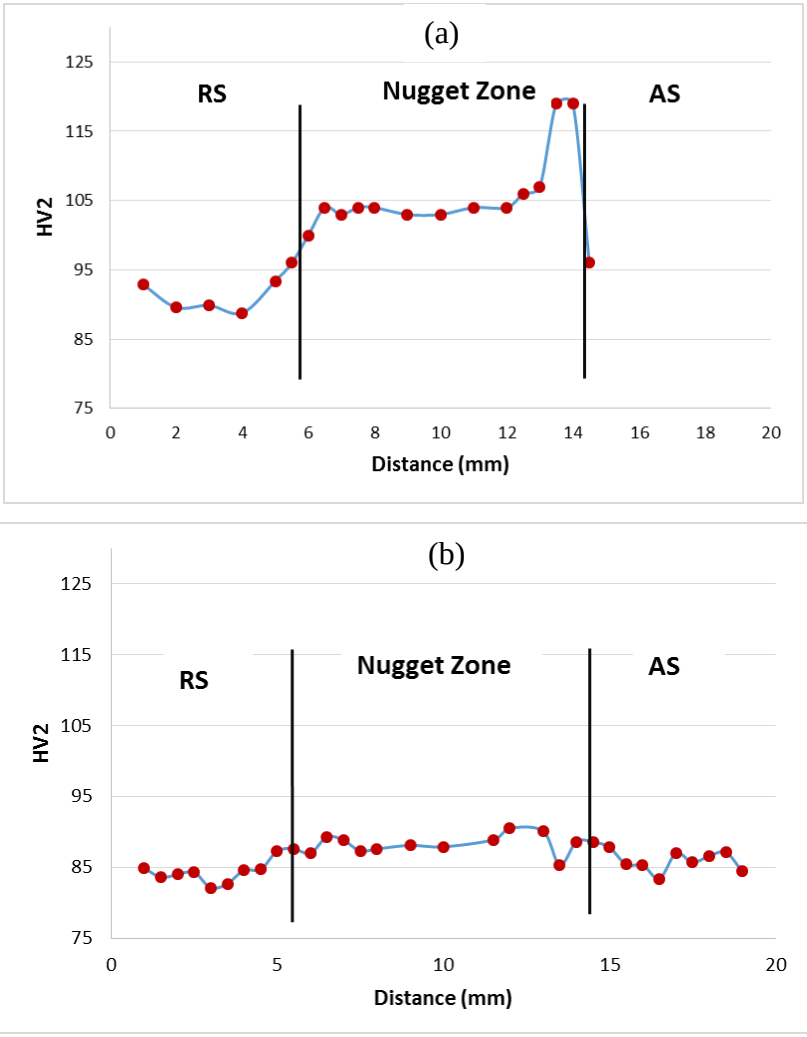

Figure 4-27. Hardness profile of the specimens after overlapping FSP process from the retreating side to advancing side of base metal

a) 290 rpm – 185 mm/min, b) 720 rpm – 100 mm/min

4.3.1.2. Hardness after Welding

Hardness profiles from the cross-section of the as-welded plate taken are shown in Figure 4-28 and Figure 4-29. The measurement line was located 2 mm below the surface of welded specimen in Figure 4-28. While the profile in Figure 4-29 is taken from the depth of 7 mm. The hardness values of the base metal, heat affected zone and weld metal 2 mm below the weld cap was recorded as 89±7 HV2, 81±3 HV2 and 75±5 HV2, respectively. The width of HAZ region was inspected to be 3mm in both sides of the fusion line of weld when measure in Figure 4-28. Considering the low level of strain hardening amount of the H111 condition, the narrowness of the HAZ is not an unexpected outcome.

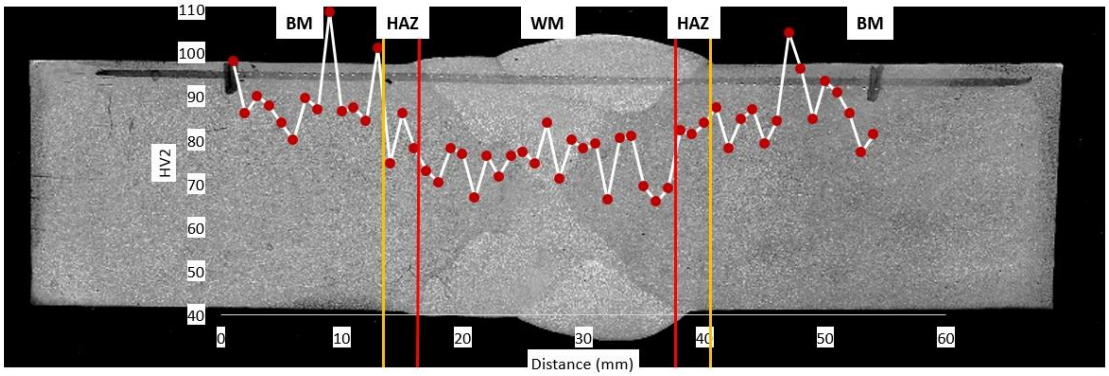

Figure 4-28. Hardness profile of the welded plate (2 mm below the surface)

The hardness values of these three regions, 7 mm under the surface, were measured as 88±1, 84±2 and 79±1 respectively for the base metal, HAZ and weld metal of the as-welded specimen. An obvious change of HAZ width towards the center of specimen was observed as it was measured to be 8 mm in Figure 4-29. The difference in HAZ width according to the thickness of the plate is explained through the cooling rate of these layers. Since the surface layers are cooled faster, the effect of heat is limited. However, for the center of the plate heat is conserved for a longer time, which results in a wide HAZ.

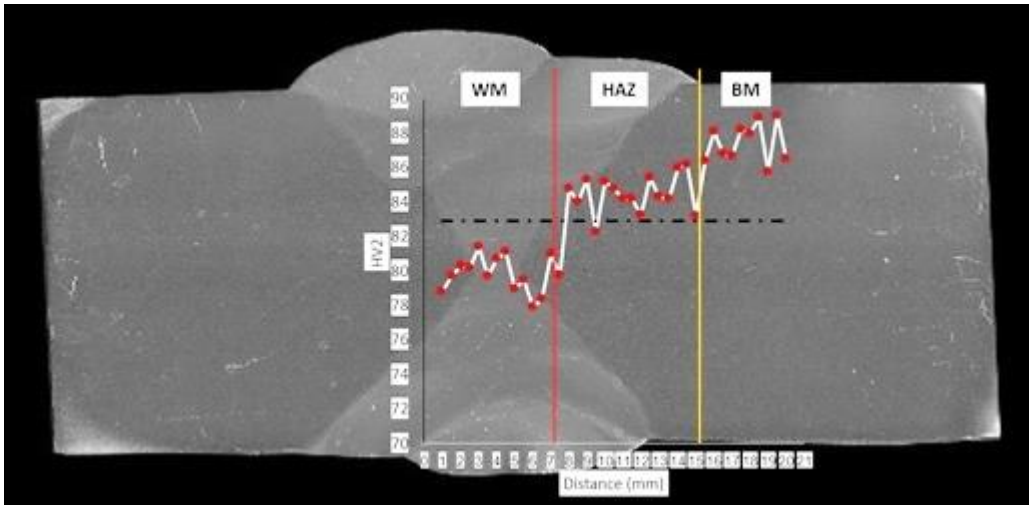

Figure 4-29. Hardness profile of the welded material (7 mm below the surface)

4.3.1.3. Hardness Profile of the FSPed and welded plate

The hardness of the FSPed and welded specimen were measured with the same methodology. In Figure 4-30 the hardness values were collected 2 mm below the surface as illustrated by the black dotted line. The hardness values are 90±6, 96±5, 91±4 and 76±4 HV2 for base metal, pre-FSPed metal, pre-FSPed HAZ and weld metal, respectively.

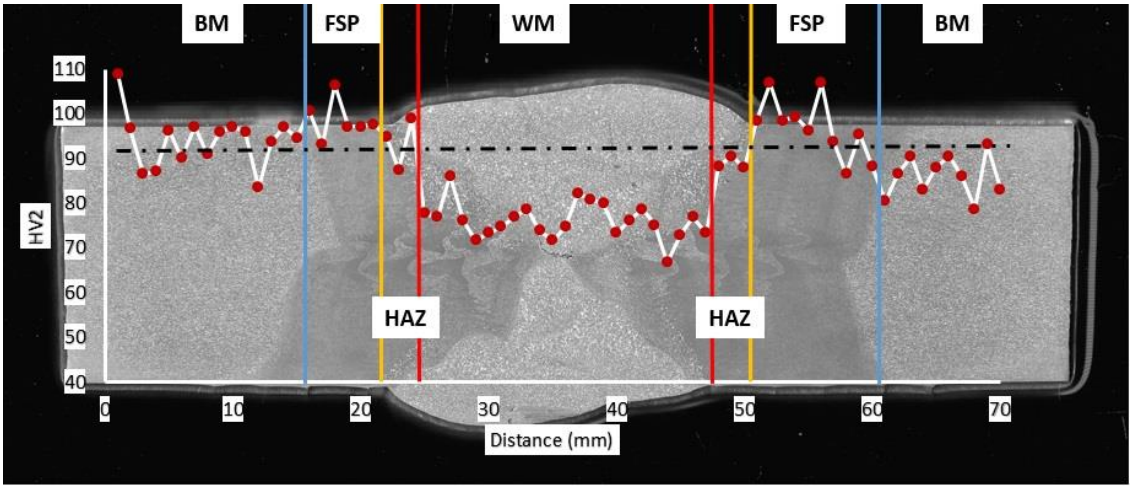

Figure 4-30. Hardness profile of the FSPed and welded plate (2 mm below surface)

As seen in Figure 4-31 the hardness values are 85±3, 89±3, 82±4 and 75±5 HV1 for the base metal, pre-FSPed metal, pre-FSPed HAZ and weld metal, respectively.

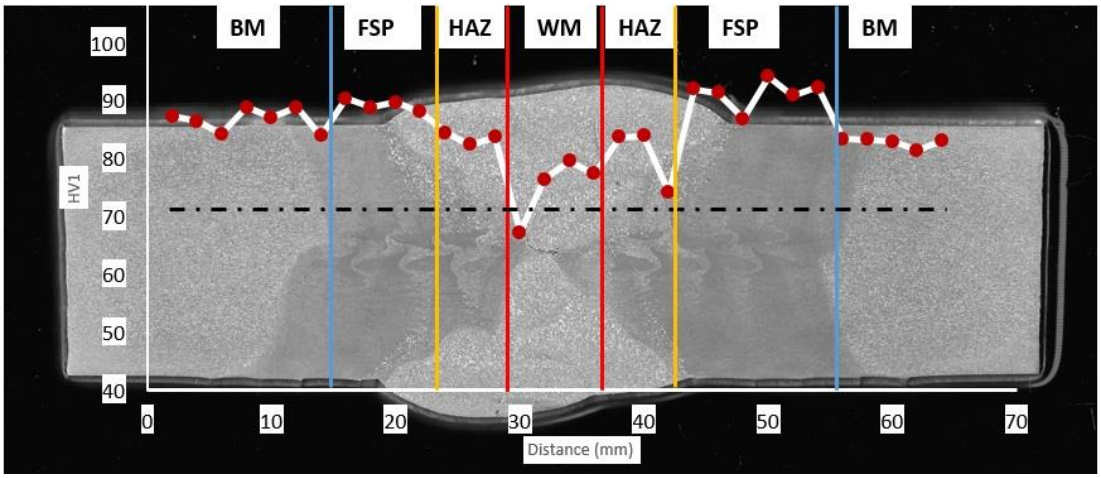

Figure 4-31. Hardness profile of the FSPed and welded plate (7 mm below the surface)

The hardness drop in the base metal is about 9 HV2, while that for the FSPed metal is less than 6 HV2. Also, towards the center of the plate, similar to welded specimen, widening of the HAZ is observed. However, in the same depth, while the HAZ of welded base metal was more than 8 mm, HAZ of FSPed metal is barely 6 mm.

4.3.2. Tensile Test

The tensile test results of the base metal and FSPed samples are given in Table.4.5.

Table.4.5. Results of the tensile tests

Material of Specimen	Yield Strength at 0.2 strain	UTS(MPa)
Base Metal Prependicular to the Rolling Direction	195±1	334±1
Base Metal Parallel to the Rolling Direction	226±0	331±1
FSPed Base Metal 720 rpm- 100 mm/min	180±4	342±1
FSPed Base Metal 290 rpm - 185 mm/min	208	343

The stress-strain curves of the specimens are shown in Figure 4-32. As it is seen from the graphs, FSPed specimens have higher tensile strengths, while their yield strengths are slightly lower than those of the base metal perpendicular to rolling direction. Since the FSP and welding were applied in the rolling direction, the comparisons were made by considering the direction perpendicular to the rolling direction.

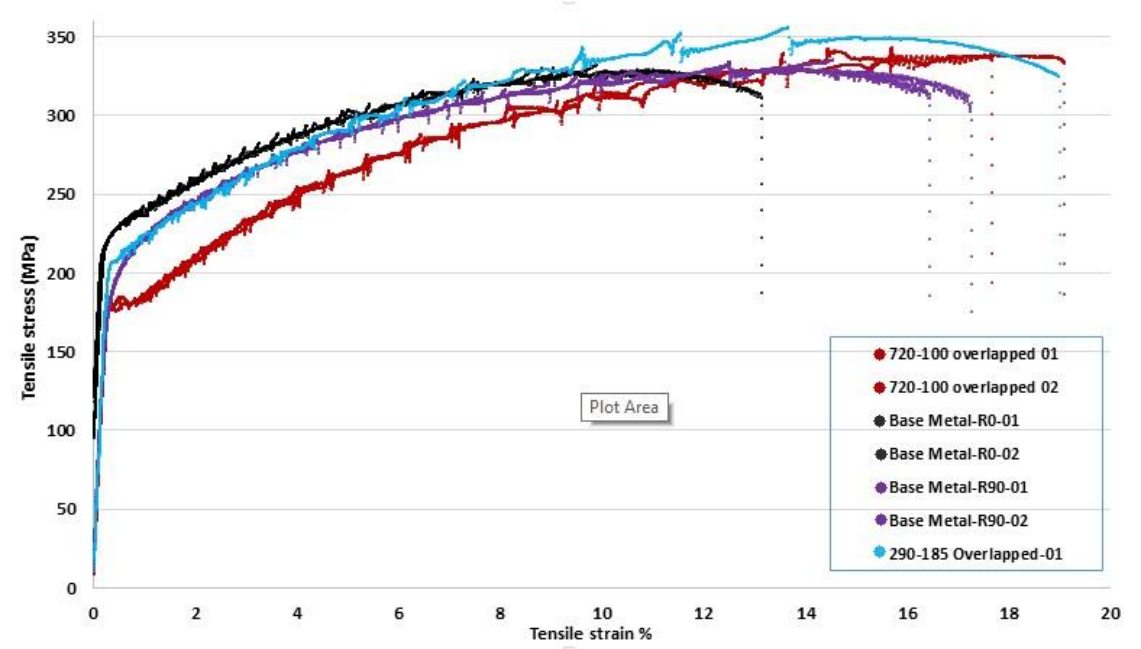

Figure 4-32. Stress-Strain curves of the samples

The tensile strength of the notched specimens in HAZ regions are presented in Table 4.6. An improvement of tensile strength is observed in the HAZ region of the FSPed plate. Investigating on the fracture surface of the specimens have shown the effect of fine grains on the formation of the dimples (Figure 4-33).

Table 4.6. Results of notch tensile tests

	Specimen Number	σ_y (MPa)	Average±Standard Deviation (MPa)
HAZ of Base Metal	1	227	235±18
	2	231	
	3	264	
	4	216	
HAZ of FSPed Metal	1	267	265±13
	2	244	
	3	219	
	4	276	

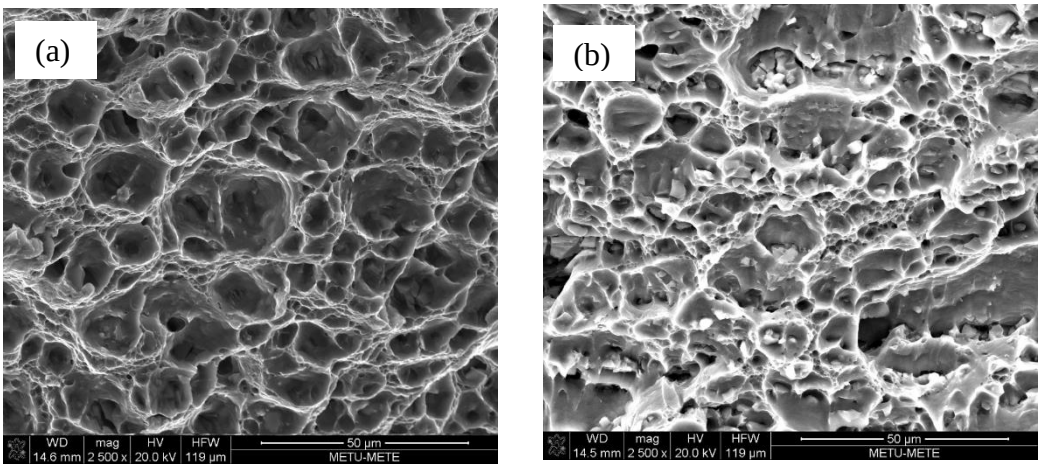

Figure 4-33. Fracture surfaces of tensile specimens
(a) HAZ of base metal, (b) HAZ of FSPed and welded metal

4.3.3. Fatigue Crack Propagation Test

Fracture surface of a compact tension specimen is illustrated in Figure 4-34. The darker grey area, starting from the notch, belongs to the pre-crack loadings, which had higher values with respect to crack loadings. The change of load caused formation of a beach mark on fracture surface.

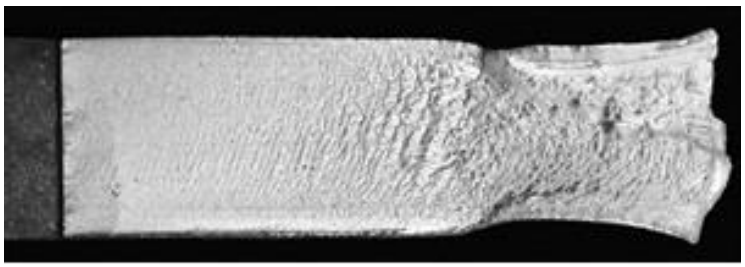

Figure 4-34. Fracture surface of the FSPed CT specimen

The data collected by CMOD and optical method were similar to each other. For each test, C and m values were calculated in the steady state region in crack growth rate versus stress intensity factor graphs. The crack length (a) versus cycle number (N) graphs for three base material, three HAZ of base metal and five HAZ of FSPed and welded plate are given in Figure 4-36, Figure 4-38 and Figure 4-40, respectively. Crack growth rate (da/dN) versus stress intensity (ΔK) graphs are given in Figure 4-37,Figure 4-39 and Figure 4-41. Both optical and CMOD data were used to maintain two graphs for each specimen. In spite of data elimination procedure, scattering of the results was still observed in a few of specimens. Figure 4-35, shows SEM images of fracture surface of FCP tests (BM3 specimen).

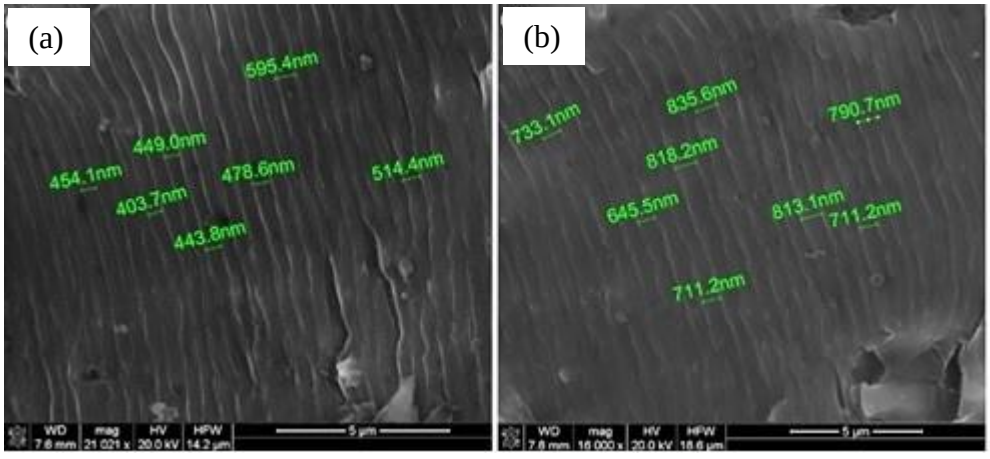

Figure 4-35. Striations and their length at a distance of
(a) 8 mm, (b) 12 mm from the pre-crack

Visual and numerical results of the crack propagation tests are presented in Figures Figure 4-36 to Figure 4-41.

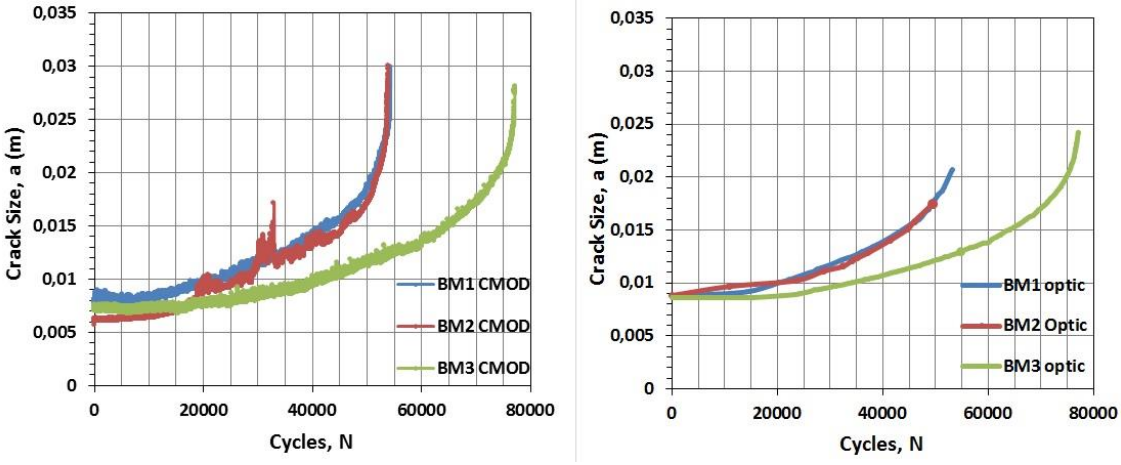

Figure 4-36. Crack length versus number of cycles curves for the base metal

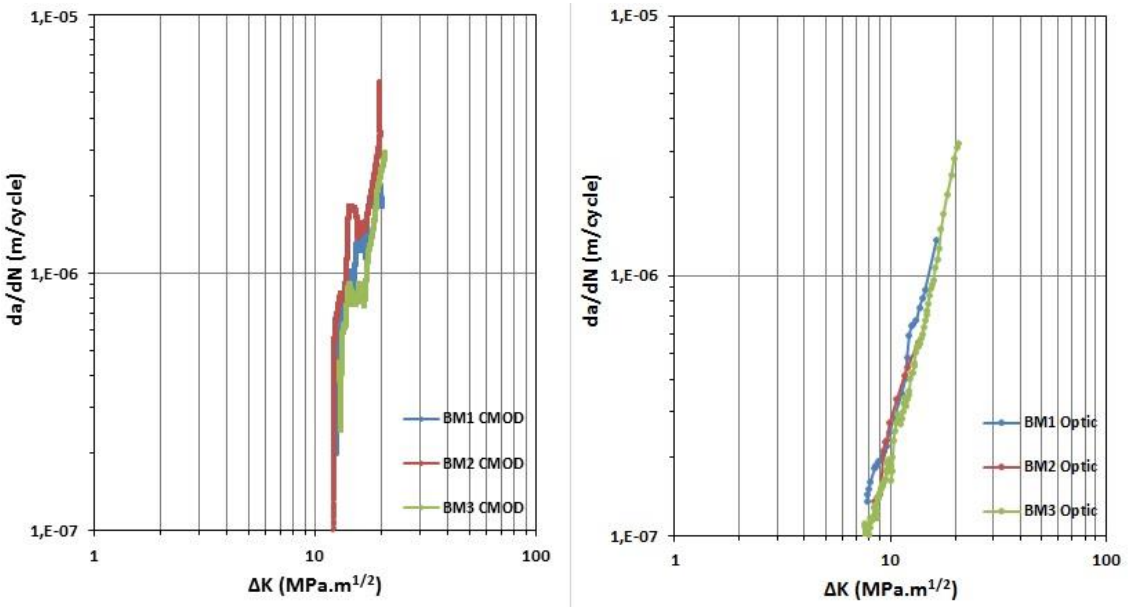

Figure 4-37. Crack growth rate versus stress intensity factor curves for the base metal

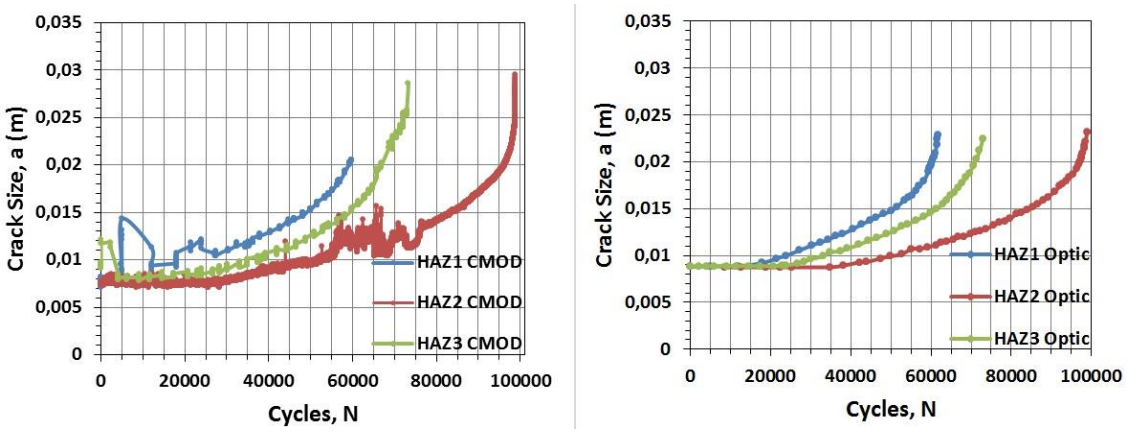

Figure 4-38. Crack length versus number of cycles curves for HAZ8888888888888888

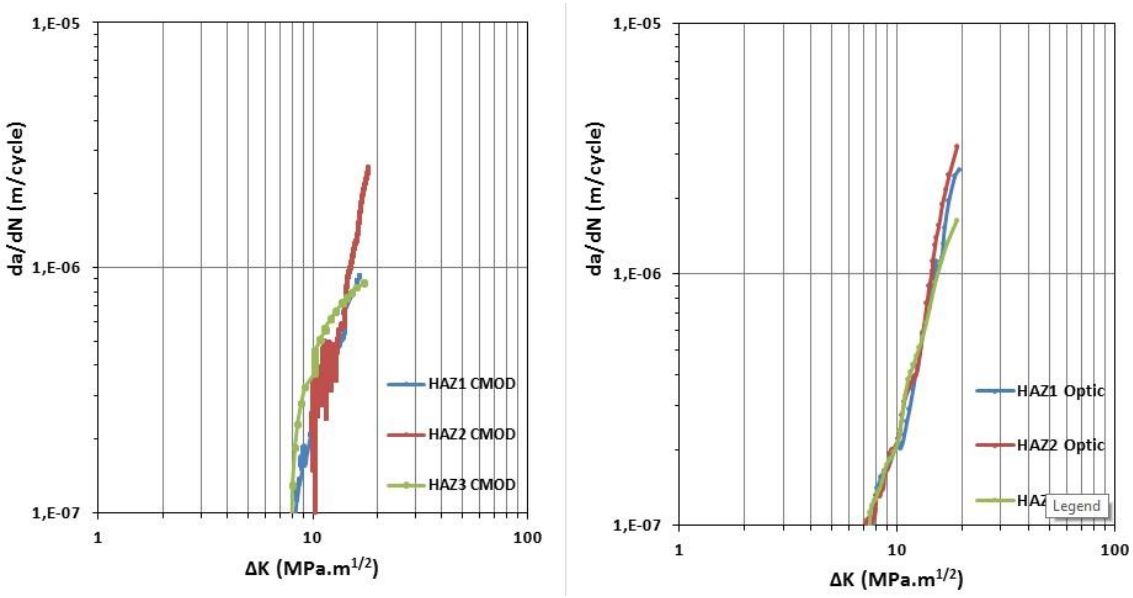

Figure 4-39. Crack growth rate versus stress intensity factor curves for the HAZ

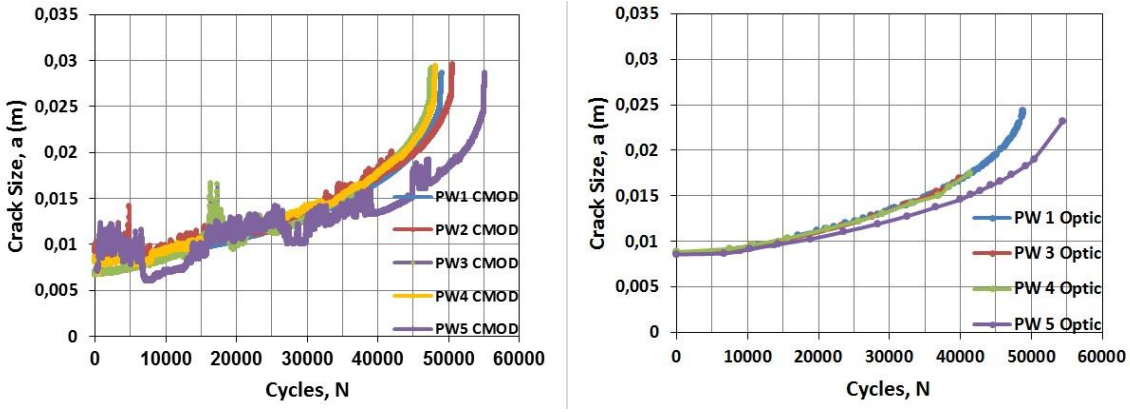

Figure 4-40. Crack length versus number of cycles curves for the HAZ of FSPed and welded plate

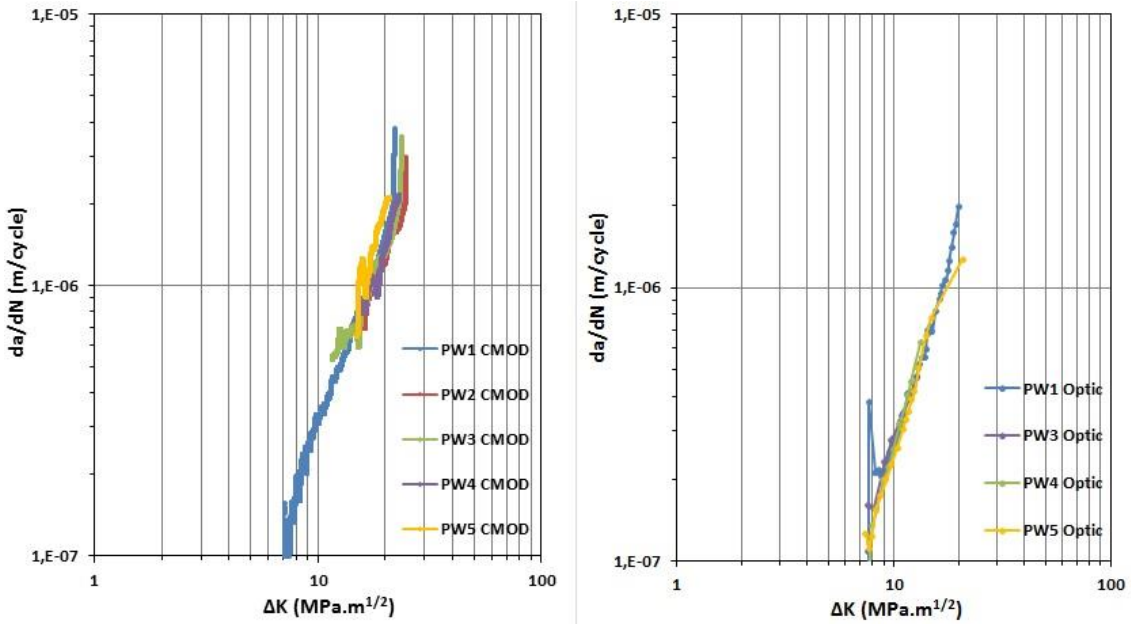

Figure 4-41. Crack growth rate versus stress intensity factor curves for the HAZ of FSPed and welded plate

da/dN versus ΔK graph of the first sample for each group is plotted for comparison purpose. Two graphs for optic and CMOD data are plotted in Figure 4-42.

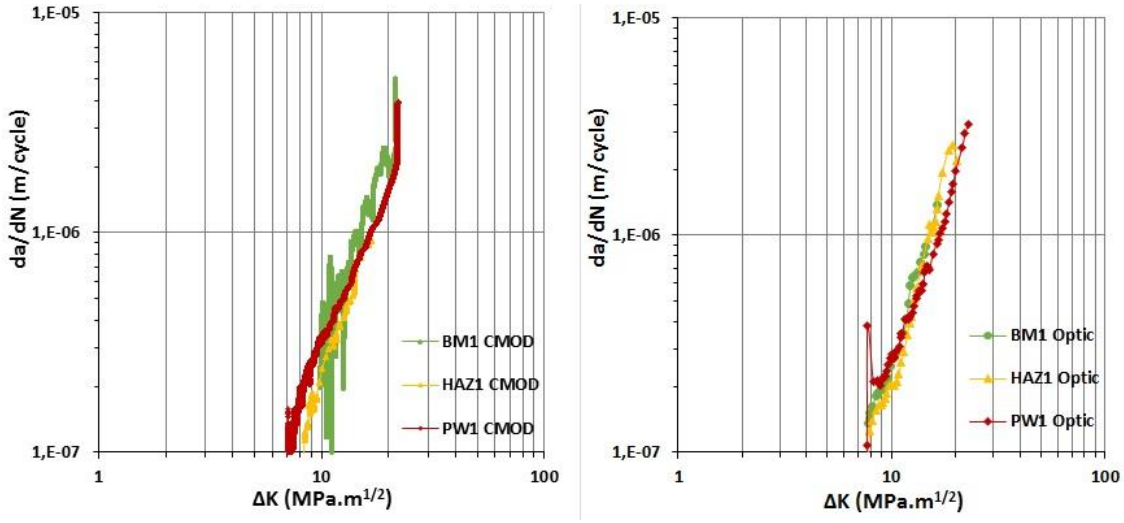

Figure 4-42. Crack growth rate versus stress intensity factor curves of the samples

The constants of Paris-Erdoğan law and the crack growth rate for the stress intensity factor of 15 for each data of each sample are stated in Table 4.7.

Table 4.7. Results of the crack growth studies

	Base Metal		**HAZ of Base Metal**		**HAZ of pre-FSPed Metal**	
	Optical	CMOD	Optical	CMOD	Optical	CMOD
Cx10^{-10} [m]	4.5±2.6	5.8±0.8	1.0±0.7	0.8±0.3	11.8±6.8	13.3±2.7
m	2.9±0.3	2.8±0.1	3.6±0.5	3.5±0.1	2.4±0.2	2.4±0.1
da/dNx10^{-6} [m/cycle] **@ ΔK=15**	1.1	1.0	1.1	1.2	0.81	0.82

In previous studies effect of the ultra-fine grains has been observed to reduce the ΔK_{th} value and provide faster FCP rates. This has been related to the roughnes induces crack closure mechanisms [42] [43]. Although in this study ΔK_{th} values were not calculated, improvement was maintained in crack growth behavoir of the specimens at second and

third stages of crack growth maintaining better values for Paris-Erdoğan law constants. Providing sufficient heat input to the plates via welding process caused moderately fine microstructure rather than ultra-fine grains.

The optimum size of the grains improved the fatigue crack propagation behavior of FSPed and welded specimens. The illustration of this manner is provided in Figure 4-43.

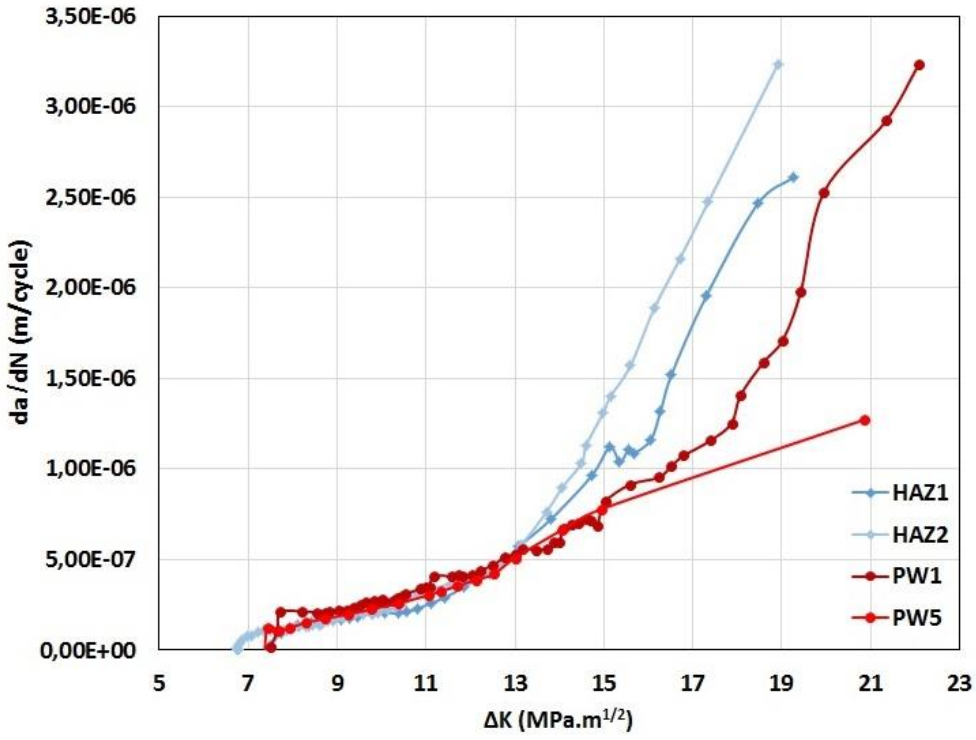

Figure 4-43. Comparison of crack growth rate versus stress intensity factor curves for HAZ of base metal (HAZ1, HAZ2) and HAZ of FSPed and welded metal(PW1, PW5)

The comparison of the grain structure for both of the HAZ specimens in the ΔK_{th} vicinity, also admits the proper size of the grains in FSPed and welded metal. Also, the illustrated side cracks in Figure 4-45 may clarify the resistance of the material against the growth of the crack.

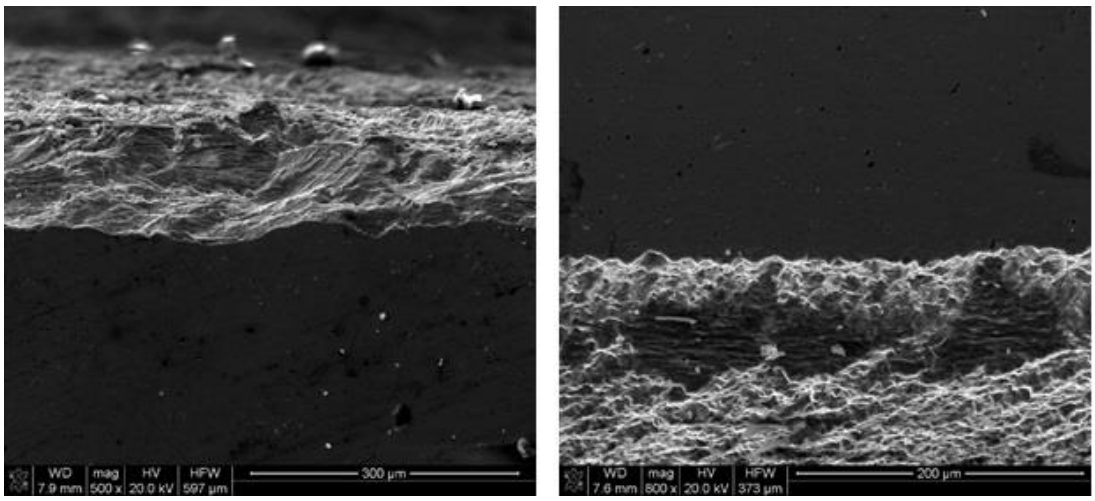

Figure 4-44. Fracture surface at the vicinity of the ΔK_{th} for
(a) HAZ of base metal, (b) HAZ of FSPed and welded metal

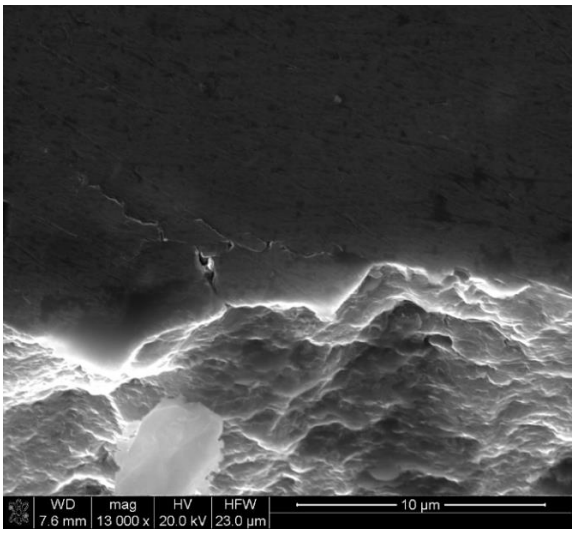

Figure 4-45. Side cracks in the fracture surface of the FSPed and welded metal at the vicinity of ΔK_{th}

Although the coarse grains and intermetallics in the HAZ of base metal assist the specimens to resist against propagation at first stage, it is a remarkable disadvantage in the second and third stages of FCP. According to previous studies, relatively fine grains

and dispersed intermetallic provide a noticeable advantage in the second and third stages. This creates more obstacles in front of the crack tip to overcome [44].

In Figure 4-46, an agglomerated brittle intermetallic particle is observed in the plastic deformation zone of the crack in the CT specimen prepared from HAZ. In the CT specimens prepared from the HAZ of FSPed welded specimens, such a formation was not encountered.

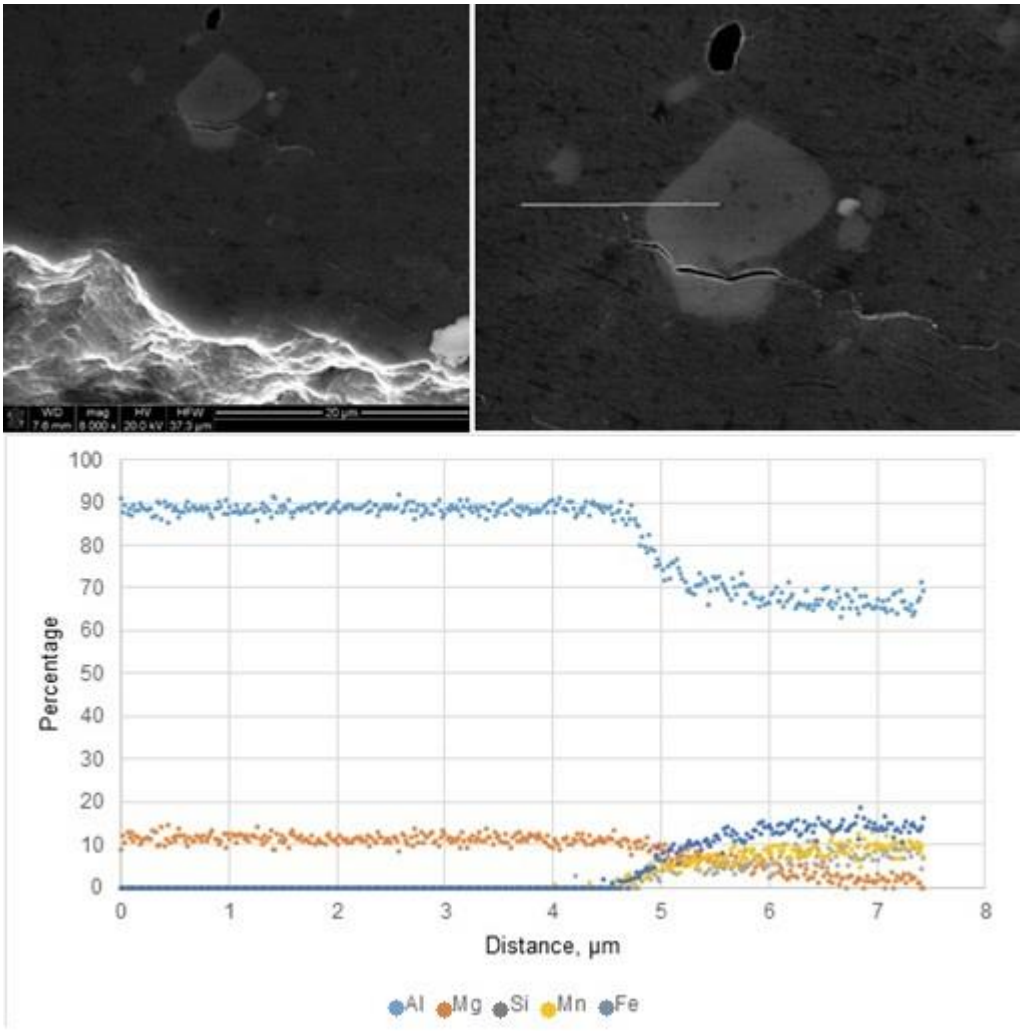

Figure 4-46. Intermetallic particle in the plastic deformation zone of the crack tip

To have a general view on the study, Table 4.8 provides comparisons for the whole features of the specimen groups.

Table 4.8. The summary of the results

	D_{grain}, μm	Yield Strength $\sigma_{0.02}$, MPa	σ_{UTS}, MPa	m	$Cx10^{-10}$, m	Hardness, HV 2
Base Metal	54	195	331	2.9	5.2	91
HAZ of Base Metal	59	-	235 (Notched)	3.6	0.9	82
FSPed Metal	1-3	204	349	--	--	92
HAZ of FSPed Metal	3-6	-	265 (Notched)	2.4	12.6	87

CHAPTER 5

CONCLUSIONS

To minimize the losses in hardness and strength and to improve the fatigue behavior in the heat affected zone (HAZ) of the welded 5083 Al-alloy plates, friction stir processing (FSP) was applied to the bevels of the plates before welding. Initially, the FSP parameters were optimized after selecting the appropriate tool. For the experimental investigations, two sample sets were prepared by gas metal arc welding in a conventional way and by gas metal arc welding after FSP. Microstructures were investigated, and average grain size, hardness, yield strength, ultimate tensile strength, and the constants of the Paris-Erdoğan equation were determined for the specimens prepared from the base metal and the HAZs of the welded plates. The following conclusions can be drawn from this particular study:

- Application of FSP with hot parameters (high rotational and low traveling speeds) causes higher heat input, and thus, coarser grains and lower hardness in comparison to the samples FSPed with cold parameters (low rotational and high travelling speeds). However, the microstructure of the sample FSPed using hot parameters is more stable under the effect of subsequent heating.
- Application of FSP before welding improves the properties of HAZ of the welded 5083 Al-alloy plates. For instance, microstructure consists of finer grains, the drops in hardness and strength are avoided, and the fatigue crack growth rate decreases in comparison to the HAZ of the conventionally welded plates.
- In the HAZ of the plates prepared by combined application of FSP and welding, the heat input to the FSPed region during welding causes local abnormal grain growth at few places, which might be affected by misorientation of grains, amount

and size of dispersed second phase particles, internal energy level of the grains, and FSP parameters. However, it does not result in a significant drop in mechanical properties if the number of exceptionally coarse grains is low.

- If fusion welding is a part of the manufacturing route of 5083 Al-alloy, FSP of the bevel regions of the plates prior to welding may significantly improve the mechanical properties of the HAZ and fatigue life of the welded component.

REFERENCES

[1] A. Ghosh and T. Bieler, Superplasticity and superplastic forming, Pennsylvania: Warrendale, 1995.

[2] R. Mishra and M. Mahoney, Friction Stir Wleding and Processing, Ohio: ASM International, 2007.

[3] S. Jana, R. Mishra, J. Baumann and G. Grant, "Effect of friction stir processing on fatigue behavior of an investment cast Al-7Si-0.6 Mg alloy," Acta Materiala, vol. 58, pp. 989-1003, 2010.

[4] G. Akçay, "Effect of Friction Stir Processing on Fracture Toughnes and Crack Growth Behaviour on Welded 5083 Grade Aluminum Plates," METU, Ankara, 2015.

[5] G. Kaufman, Aluminum alloys and Tempers, Materials Park O.H.: ASM International, 2000.

[6] R. Singh, Applied Welding Engineering, Butterworth-Heinemann: Elsevier, 2012.

[7] M. Ashby and D. Jones, Engineering Material 2 An Introduction to Microstructure, Processing and Design, Cambridge: Butterworth-Heinemann, 1999.

[8] J. Adams and e. al, "Volume 2 Properties and Selction of Non-ferrous Alloys," in ASM Handbook, Ohio, ASM International, 1992.

[9] A. Haddadzadeh, M. Ghaznavi and A. Kokabi, The effect of gas tungsten arc welding and pulsed-gas tungsten arc welding processes' parameters on the heat affected zone-softening behavior of strain-hardened Al–6.7Mg alloy, Waterloo: Elsevier, 2013.

[10] C. Dorum, O. Lademo, O. Myhr, T. Berstad and O. Hopperstad, "Finite element analysis of plastic failure in heat-affected zone of welded aluminium

connections," Elsevier, Trondheim, 2009.

[11] R. Nandan, T. DebRoy and H. Bhadeshia, "Recent advances in friction-stir welding – Process,weldment structure and properties," Progress in Materials Science, vol. 53, p. 980–1023, 2008.

[12] Z. Ma, S. Sharma and R. Mishra, "Effect of friction stir processing on the microstructure of cast A356 aluminum," Materials Science and Engineering , vol. A 433, p. 269–278, 2006.

[13] F. Lefebvre, S. Ganguly and I. Sinclair, "Micromechanical aspects of fatigue in a MIG welded aluminium airframe alloy," Materials Science and Engineering, vol. 397, p. 338–345, 2005.

[14] S. Rajakumar, C. Muralidharan and V. Balasubramanian, "Predicting tensile strength, hardness and corrosion rate of friction stir welded AA6061-T6 aluminium alloy joints," Materials and Design, vol. 32, p. 2878–2890, 2011.

[15] S. Zimmer, L. Langlois, J. Laye and J. Claude, "Using the plunging and welding process windows to determine a FSW means of production," Advanced Materials Research, Vols. 89-91, pp. 697-702, 2010.

[16] M. Vukčević, S. Savićević, M. Janjić and N. Šibalić, "Measurement in friction stir welding process," in Trends in the Development of Machinery and Associated Technology", Prague, 2011.

[17] A. Reynolds, "Flow visualization and simulation in FSW," Scripta Materialia, vol. 58, p. 338–342, 2008.

[18] H. Schmidt, T. Dickerson and J. Hattel, "Material flow in butt friction stir welds in AA2024-T3," Acta Materialia , vol. 54 , p. 1199–1209, 2006.

[19] P. Surendrababu, A. G. Krishna and C. S. Rao, "Material Flow Behaviour in Friction Stir Welding Process-A Critical Review on Process Parameters and Modeling Methodologies," International Journal of Emerging Technology and Advanced Engineering, vol. 3, no. 6, 2013.

[20] K. Jata and S. Semiatin, "Continuous dynamic recrystallization during friction stir welding of high strength aluminum alloys," Scripta material, vol. 43, p. 743–749, 2000.

[21] C. Sellars and W. McTegart, "On the mechanism of hot deformation," Acta Metalurgica, vol. 14, no. 9, pp. 1136-1138, 1966.

[22] T. Sheppard and D. S. Wright, "Determination of flow stress: Part 1 constitutive equation for aluminium alloys at elevated temperatures," Metals Technology, vol. 9, no. 1, pp. 215-223, 1979.

[23] T. Sheppard and D. S. Wright, "Determination of flow stress: Part 2 radial and axial temperature distribution during torsion testing," Metals Technology, vol. 6, no. 1, pp. 224-229, 79.

[24] C. Zener and J. H. Hollomon, "Effect of Strain Rate upon Plastic Flow of Steel," Applied Physics, vol. 15, pp. 22-32, 1944.

[25] O. Dada, C. Polese and L. Cornish, "Relationship between Residual Stresses and Welding Rates in Friction Stir Welded AA6056-T4," in International MultiConference of Engineers and Computer Scientists, Hong Kong, 2013.

[26] D. Richards, P. Prangnell, S. Williams and P. Withers, "Global mechanical tensioning for the management of residual stresses in welds," Materials Science and Engineering: A, vol. 489, no. 1-2, p. 351–362, 2008.

[27] H. Lombard, D. Hattingh, A. Steuwer and M. James, "Optimising FSW process parameters to minimise defects and maximise fatigue life in 5083-H321 aluminium alloy," Engineering Fracture Mechanics, vol. 75, no. 3-4, p. 341–354, 2008.

[28] "Engineering Edge," Engineering Supples and Book Store , 2000. [Online]. Available: http://www.engineersedge.com/material_science/fatigue_crack_growth_analysis_review_10071.htm. [Accessed 22 11 2015].

[29] P. Paris and F. Erdogan, "A Critical Analysis of Crack Propagation Laws," Basic Engineering, vol. 85, no. 4, pp. 528-533, 1963.

[30] R. Smith, Basic Fracture Mechanics : Including and Introduction to Fatigue, Oxford: Butterworth-Heinemann Ltd, 1991.

[31] L. Canale, R. Mesquita and G. Totten, Failure Analysis of Heat Treated Steel Components, Ohio: ASM International, 2008.

[32] R. Ambriz and D. Jaramillo, "Mechanical Behavior of Precipitation Hardened Aluminum Alloys Welds," in Light Metal Applications, Catarina,, Instituto Politécnico Nacional CIITEC-IPN, 2014.

[33] Y. Chena, H. Dinga, J. Lib, Z. Caia, J. Zhaoc and W. Yanga, "Influence of multi-pass friction stir processing on the microstructure and mechanical properties of Al-5083 alloy," Materials Science and Engineering: A, vol. 650, p. 281–289, 2016.

[34] F. Humphreys, "A unified theory of recovery, recrystallization and grain growth, based on the stability and growth of cellular microstructures—I. The basic model," Acta Materialia, vol. 45, no. 10, p. 4231–4240, 1997.

[35] F. Humphreys, "A unified theory of recovery, recrystallization and grain growth, based on the stability and growth of cellular microstructures—II. The effect of second-phase particles," Acta Materialia, vol. 45, no. 12, p. 5031–5039, 1997.

[36] P. Sivaraja, D. Kanagarajana and V. Balasubramanianb, "Effect of post weld heat treatment on tensile properties and microstructure characteristics of friction stir welded armour grade AA7075-T651 aluminium alloy," Defence Technology, vol. 10, no. 1, p. Pages 1–8, 2014.

[37] A. El-Danaf and M. M. El-Rayes, "Microstructure and mechanical properties of friction stir welded 6082 AA in as welded and post weld heat treated conditions," Materials & Design, vol. 46, p. 561–572, 2013.

[38] Y. Chen, H. Ding, J. Li, J. Zhao, M. Fu and X. Li, "Effect of welding heat input and post-welded heat treatment on hardness of stir zone for friction stir-welded 2024-T3 aluminum alloy," Transactions of Nonferrous Metals Society of China, vol. 25, no. 8, p. 2524–2532, 2015.

[39] J. D. Verhoeven, Fundamentals of Physical Metallurgy, New York: John Wiley and Sons, 1975.

[40] P. Edwards and M. Ramulu, "Fatigue performance of Friction Stir Welded Ti–6Al–4V subjected to various post weld heat treatment temperatures," International Journal of Fatigue, vol. 75, pp. 19-27, 2015.

[41] M. Peel, A. Steuwer, M. Preuss and P. Withers, "Microstructure, mechanical properties and residual stresses as a function of welding speed in aluminium

AA5083 friction stir welds," Acta Materialia, vol. 51, p. 4791–4801, 2003.

[42] P. S. Pao et al., "Fatigue Crack Propagation in Ultrafine Al-Mg Alloy," International Journal of Fatigue, vol. 27, pp. 1164-1169, 2005.

[43] T. Hanlon, T. Kwon and Y. Suresh, "Grain Size Effects on the Fatigue Response of Nano-Crystalline Metals," Scripta Materiala, vol. 49, pp. 675-680, 2003.

[44] J. Donald, G. Bray and R. Bush, "An evaluation of the Adjusted Compliance Ratio Technique for Determining the Effective Stress Intensity Factor," American Society for Testing and Materials, vol. 29, pp. 674-695, 1999.

[45] W. Hosford, Physical Metallurgy, Boca Raton: Taylor and Francis, 2005.

[46] E. K. Center, "http://www.esab.ca/ca/en/education/blog/understanding-the-aluminum-alloy-designation-system.cfm," ESAB, 26 March 2014. [Online].

[47] "EN ISO 17636-1 Non-destructive testing of welds - Radiographic testing - Part 1: X- and gamma-ray techniques with film," 2013.

[48] A. Orozco-Caballeroa, S. Menonb, C. Cepeda-Jiméneza, P. Hidalgo-Manriquea, T. McNelleyb, O. Ruanoa and F. Carreñoa, "Influence of microstructural stability on the creep mechanism of Al–7 wt% Si alloy processed by equal channel angular pressing," Materials Science and Engineering: A, vol. 712, p. 162–171, 2014.

[49] T. Anderson, "Fracture Mechanics Fundamentals and Applications," CRC Press, 1995.

[50] J. Barsom and S. Rolfe, Fracture and Fatigue Control in Structures, Prentice Hall, 1987.

[51] S. J. Yuan, Z. L. Hu and X. S. Wang, "Formability and microstructural stability of friction stir welded Al alloy tube during subsequent spinning and post weld heat treatment," Materials Science&Engineering, vol. A558, p. 586–591, 2012.